



Rational synthesis of $\text{Bi}_x\text{Fe}_{1-x}\text{VO}_4$ heterostructures impregnated sulfur-doped g- C_3N_4 : A visible-light-driven type-II heterojunction photo (electro)catalyst for efficient photodegradation of roxarsone and photoelectrochemical OER reactions

Sridharan Balu^a, Yi-Lun Chen^a, Shih-Wen Chen^b, Thomas C. -K. Yang^{a,b,*}

^a Department of Chemical Engineering and Biotechnology, National Taipei University of Technology, Taipei 106, Taiwan, ROC

^b Precision Analysis and Materials Research Centre, National Taipei University of Technology, Taipei 106, Taiwan, ROC

ARTICLE INFO

Keywords:

$\text{Bi}_x\text{Fe}_{1-x}\text{VO}_4$
Sulfur-doped CN
Photoelectrochemical
Water-splitting
Photodegradation
Roxarsone
Type-II heterojunction

ABSTRACT

Metal vanadate (MVO_4) and graphitic carbon nitride (g- C_3N_4) semiconductor materials have attracted much interest due to their tremendous physicochemical and photocatalytic performances. In this prospect, $\text{Bi}_x\text{Fe}_{1-x}\text{VO}_4$ were prepared by mixing cation precursors (Bi and Fe) in different proportions ($x = 0.7; 0.5; 0.3$) via a simple one-pot hydrothermal route and impregnated on the surface of sulfur-doped g- C_3N_4 (SCN) to attain a wide range of solar absorption and effective charge separation. Several spectroscopic techniques were used to analyze the physicochemical and optoelectronic properties of as-synthesized photocatalysts. The photocatalytic activities of as-synthesized photocatalysts were evaluated by photoelectrochemical oxygen evolution reactions (OER) and photodegradation of roxarsone (ROX). This work aims to investigate the formation, photocatalytic performance, and rational mechanism of $\text{Bi}_x\text{Fe}_{1-x}\text{VO}_4/\text{SCN}$ photocatalytic nanocomposites. Among different $\text{Bi}_x\text{Fe}_{1-x}\text{VO}_4$ ($x = 0.7; 0.5; 0.3$), the $\text{Bi}_{0.5}\text{Fe}_{0.5}\text{VO}_4/\text{SCN}$ (Bi/Fe = 0.5) nanocomposite results in 85.66% of ROX photodegradation within 90 mins under visible-light irradiation. The photocatalytic performance of the nanocomposite is about 2.49, 2.87, 3.48 folds higher than that of pristine g- C_3N_4 , BiVO_4 , and FeVO_4 samples, respectively. The photoelectrochemical OER results suggest the higher photocurrent density at 1.23 V (vs NHE) was achieved by $\text{Bi}_{0.5}\text{Fe}_{0.5}\text{VO}_4/\text{SCN}$ (0.987 mA cm^{-2}) nanocomposite, and which is 16.73, 5.11, and 6.16 times higher than that of CN (0.059 mA cm^{-2}), BiVO_4 (0.193 mA cm^{-2}), and FeVO_4 (0.160 mA cm^{-2}), respectively. The XPS and photoelectrochemical (PEC) analysis depict the higher donor densities (N_D) and excellent charge separations through type-II heterojunction of the $\text{Bi}_x\text{Fe}_{1-x}\text{VO}_4/\text{SCN}$ nanocomposite.

1. Introduction

Last several decades, the artificial photosynthesis process has received significant interest due to the simple process of solar energy production. Photochemical and photoelectrochemical (PEC) processes effectively convert direct solar power to chemical energy [1,2]. Among, many industries have utilized the PEC water-splitting technique to produce H_2 and O_2 for industrial purposes. Compared to PEC water splitting, the steam reforming technology effectively produces H_2 around ~ 55 million metric tons every year. The steam reforming process also produces CO_2 as a by-product of around ~ 400 million metric tons annually, about 1.3% of the total CO_2 emission [3,4]. For the PEC

water splitting reaction, a semiconductor catalyst with proper band alignment equal to or less than 1.23 eV was utilized to enhance light-harvesting and PEC efficiency. Besides, the semiconductor-mediated PEC water splitting reactions offers a lower potential for higher conversion rates at low temperatures using cost-effective photoanode/photocathode materials [5–7]. Therefore, still some developments are needed to increase the light-harvesting, efficiency, stability, and durability of the photocatalyst materials used in PEC water-splitting processes.

As a consequence of various natural processes such as geochemical weathering, volcanic deposition, mineral leaching and soil erosion processes, arsenic-containing species seem to exist naturally in our

* Correspondence to: Department of Chemical Engineering and Biotechnology, National Taipei University of Technology, No. 1, Section 3, Chung-Hsiao E. Rd., Taipei 10608, Taiwan, ROC.

E-mail address: ckyang@mail.ntut.edu.tw (T.C.-K. Yang).

<https://doi.org/10.1016/j.apcatb.2021.120852>

Received 8 June 2021; Received in revised form 20 October 2021; Accepted 25 October 2021

Available online 29 October 2021

0926-3373/© 2021 Elsevier B.V. All rights reserved.

water systems, including lakes, rivers, ponds and reservoirs. Roxarsone (4-hydroxy-3-nitrophenylarsonic acid) is an aromatic organoarsenic contained antibiotic drug. It has been widely used as a feed additive drug in poultry and swine farms to control intestinal parasites and promote a fast growth rate. In addition, several drugs containing organoarsenic compounds have been used to treat serious diseases, including myeloma, acute promyelocytic leukemia, acute and chronic myeloid leukemia [8, 9]. Also, some organoarsenic compounds have been used as herbicides, pesticides, insecticides (such as monosodium methanearsonate, sodium salt of cacodylic acid, disodium methanearsonate, and calcium acid methanearsonate), and fungicides [10,11]. Therefore, it is considered a source of arsenic poisoning in the water system near some large poultry. According to the relative redox potentials and the pH of the water system, the oxidation states of arsenic species varies from 3^- to 5^+ . The arsenite (As^{3+}) and arsenate (As^{5+}) are common, and thermodynamically stable oxidation forms are present in the water resources. According to the World Health Organization report, arsenic content present in the drinking water is limited and should not exceed < 10 ppb to minimize arsenic poisoning. So far, various methods have been studied to remove roxarsone (ROX) from the contaminated water system, such as adsorption, electrocoagulation, photocatalysis, and photolysis [12–15]. Among them, the photocatalytic degradation technique has immense attention owing to numerous advantages, such as low toxicity, high photoactivity, high efficiency, inertness, and high stability [16].

So far, the metal-vanadate (MVO_4) nanoparticles/nanocomposites have been attracted much interest in the scientific community due to their remarkable photocatalytic properties, such as narrow bandgap energy ($E_g = 2.1$ – 2.5 eV), high optical absorbance, stability, high electrochemical activity, and non-toxic nature. In specific, the MVO_4 has excellent solar harvesting possessions (500–600 nm), which makes it an ideal candidate for environmental remediation and energy applications. Bismuth vanadate ($BiVO_4$), an n-type metal-oxide-semiconductor ($E_g = 2.4$ – 2.5 eV), has been emerged as an excellent photoanode material in the field of photocatalytic/photoelectrochemical (PEC) water splitting. On the other hand, iron vanadate ($FeVO_4$), also an n-type metal-oxide-semiconductor having a narrow bandgap value of ($E_g = 2.0$ – 2.1 eV) [17]. The apparent quantum yield (AQY) efficiency of $BiVO_4$ was limited because of its high E_g value, which is decreased by forming an $M_xM_{1-x}VO_4$ ($M_x = Bi$ and $M_{1-x} = Fe$) mixture by combining with another metal cation. The addition of a suitable metal cation could shift the VB and CB positions of $BiVO_4$ to form a heterojunction with notably higher optical absorbance and lower E_g with enhanced photoelectrochemical activities. Several previous reports have demonstrated the lowering of the bandgap of $BiVO_4$ are $BiZn_2VO_6$ and $BiCu_2VO_6$, by combining Cu/Bi and Zn/Bi. Compared to the pristine $BiVO_4$, the $BiZn_2VO_6$ and $BiCu_2VO_6$ resulted in higher light absorption > 600 nm and enhanced photocatalytic activities [18–21]. More recently, Zhang et al. have reported synthesizing mesoporous $Bi_xFe_{1-x}VO_4$ heterojunction films via electrospinning technique for solar water splitting, which results in extended optical absorption and enhanced photoelectrochemical activities owing to the tremendous catalytic activity of the mixed cations [22].

Over the past several decades, the graphitic carbon nitride ($g-C_3N_4$), a metal-free organic-inorganic semiconducting polymer (n-type) material, has received much attraction in the research field due to its remarkable physicochemical properties. Typically, the $g-C_3N_4$ has been synthesized by pyrolysis or polycondensation reactions using nitrogen-rich precursors such as urea, thiourea, melamine, dicyandiamide, and cyanamide [23,24]. Furthermore, the low toxicity, chemical/thermal stabilities, and cost-effectiveness of $g-C_3N_4$ make it to be an engaging catalyst material in the photocatalytic field such as photocatalytic/photoelectrochemical water splitting reactions, organic degradations, carbon dioxide (CO_2) reduction, water treatments, heavy metal removal, and dye-sensitized solar cells. The conduction band (CB) of the $g-C_3N_4$ is located at around -1.2 V (vs NHE at pH7), which is more negative than that of the photoreduction potentials of methanol (-0.38

V), formaldehyde (-0.48 V), methane (-0.24 V), formic acid (-0.61 V), and ethanol (-0.33 V) produced by photocatalytic CO_2 reduction. Also, the valance band (VB) of the $g-C_3N_4$ is located more positive (1.47 V) and thus favors the photocatalytic water oxidation reactions [25].

The E_g value of $g-C_3N_4$ lies between 2.6 and 2.8 eV, which favors the visible-light absorbance in small extends up to ~ 465 nm. It also has faster recombination rates of photogenerated charge carriers, limited surface area, insufficient electrical conductivity, and poor photocatalytic activities [26]. In order to overcome the limitations of $g-C_3N_4$ in photocatalysis, it has been modified by doping of metals/non-metals, coupling with metal oxides, and metal sulfide semiconductors. Also, the layered polymeric structure of $g-C_3N_4$ creates an enormous variety of prospects to deposit different elements and impurity atoms into the backbone to modify its electronic structures [27]. In particular, non-metals such as sulfur (S), oxygen (O), boron (B), and phosphorous (P) doped $g-C_3N_4$ exhibit enhanced optical absorbance as well as increased photogenerated charge separation rates. Therefore, the non-metal doping is a facile eco-friendly approach devoid of any additional templates to improve the photocatalytic activity of $g-C_3N_4$ by creating vacant sites, modifying the morphology, and narrowing bandgap energies [28]. Owing to the high charge resistance between heptazine units, the carrier mobility of $g-C_3N_4$ decreases. Consequently, the doping of non-metals resulting in the sharing of either an occupied orbital with extra electrons (P and S) or an empty orbital (B) with the π -conjugated structure will lead to higher delocalization of π electrons in the heptazine network, which also increases carrier mobility of $g-C_3N_4$ [27].

In our current work, we performed a one-pot hydrothermal synthesis of $Bi_xFe_{1-x}VO_4$ heterostructures by mixing cation precursors (Bi and Fe) in different stoichiometric proportions ($x = 0.7; 0.5; 0.3$) without adding any surfactants. On the other hand, CN and SCN were prepared by direct thermal pyrolysis of dicyandiamide and thiourea, respectively. The $Bi_xFe_{1-x}VO_4$ /SCN nanocomposite was prepared using the total solvent evaporation and impregnation technique. The mixed-phase $Bi_xFe_{1-x}VO_4$ heterostructures expands the visible-light-harvesting, photogenerated charge carrier separation and transfer efficiencies. The photocatalytic activities of as-synthesized photocatalysts were evaluated by photoelectrochemical OER reactions and photodegradation of roxarsone. The formation of $Bi_xFe_{1-x}VO_4$ heterostructure improves the optical absorption and helps to tune the bandgap energy. Besides, several characterizations examined the physicochemical, optoelectronic, and photocatalytic activities of the $Bi_xFe_{1-x}VO_4$ /SCN nanocomposites and the plausible type-II heterojunction charge transfer mechanism was discussed. The photoelectron spectroscopy and several photoelectrochemical analyses also confirm heterojunction formation, excellent charge transfer, and charge separation on the $Bi_xFe_{1-x}VO_4$ /SCN photo(electro)catalyst.

2. Experimental section

2.1. Materials and methods

Bismuth(III) nitrate pentahydrate ($Bi(NO_3)_3 \cdot 5H_2O$), iron(III) nitrate nonahydrate ($Fe(NO_3)_3 \cdot 9H_2O$), ammonium metavanadate (NH_4VO_3), dicyandiamide ($C_2N_4H_4$), thiourea (CH_4N_2S), ethyl alcohol (CH_3CH_2OH), isopropyl alcohol ($CH_3CHOHCH_3$), nafion ($C_7HF_{13}O_5S \cdot C_2F_4$), methyl alcohol (CH_3OH), sodium sulfate (Na_2SO_4), sodium sulfide (Na_2SO_3), sodium hydroxide ($NaOH$), potassium ferrocyanide ($K_4[Fe(CN)_6]$), potassium phosphate monobasic (KH_2PO_4), potassium ferricyanide ($K_3[Fe(CN)_6]$), di-potassium hydrogen phosphate (K_2HPO_4), and potassium chloride (KCl) were analytical grades obtained from Sigma-Aldrich and used without any further purifications. Deionized water (DI) was used as a solvent throughout the experimental reactions unless otherwise specified.

The optical absorbance and electronic bandgap energies of as-synthesized photocatalysts were analyzed by UV-Visible diffuse reflectance spectroscopy (UV-DRS) using UV-Vis-NIR Spectrophotometer

connected with 150 mm UV–Vis/NIR Integrating Sphere, Jasco, V-770, Japan; and photoluminescence (PL) studies were conducted using 266 nm exciting laser source at room temperature by UniRAM, Micro-PL Spectrophotometer, UniNanoTech Co., Ltd. South Korea. The morphological and structural characterizations of the materials were studied using field-emission scanning electron microscopy (FESEM) by JSM 7610F, JEOL Ltd. Japan, and Raman spectroscopy by Confocal Micro-Raman Spectrum ACRON, UniNanoTech, Ltd. South Korea. The chemical states and composition of the synthesized materials and nanocomposites were analyzed by X-ray photoelectron spectrophotometer (XPS) by JPS 9030, JEOL Ltd. Japan; and Fourier-transform infrared microscopic spectrometer (FT-IR) by PerkinElmer Frontiers, Spotlight 200i, UK. The crystallite phases of as-prepared materials were confirmed by an X-ray diffractometer (XRD, CuK α radiation, $\lambda = 1.5406 \text{ \AA}$) using Malvern PANalytical Empyrean, The Netherlands. The CHI electrochemical workstation with a standard three-electrode system was used for the photoelectrochemical experiments. Where the Ag/AgCl (sat. NaCl), a sample coated indium-tin-oxide glass plates (ITO, 1 cm^2), and a platinum wire (Pt) was used as a reference, working, and counter electrodes, respectively. For the photocatalytic and photoelectrochemical reactions, a 350 W mercury-xenon (Hg-Xe) lamp was utilized as a simulated visible-light source.

2.2. Synthesis of *g*-C₃N₄ (CN) and sulfur-doped *g*-C₃N₄ (SCN)

The pristine CN has been synthesized by thermal polycondensation of dicyandiamide [29]. In brief, 3 g of dicyandiamide was taken in a covered crucible and allowed into a muffle furnace for 3 h at 550 °C (heating ramp rate 3 °C/min). The same procedure has been adopted for the synthesis of SCN using thiourea instead of dicyandiamide. After the reaction, the obtained yellow-colored CN and SCN products were finely ground using an agate mortar.

2.3. Synthesis of $\text{Bi}_x\text{Fe}_{1-x}\text{VO}_4$ heterostructures

For a typical one-pot synthesis of $\text{Bi}_x\text{Fe}_{1-x}\text{VO}_4$ ($x = 0.7, 0.5, 0.3$), different stoichiometric ratios of Bi (x) and Fe ($1-x$) precursors were dissolved in 45 mL of deionized water and sonicated for 30 min. On the other hand, 0.526 g of ammonium metavanadate dissolved in 45 mL deionized water and sonicated for 30 min. After that, the homogeneous mixture of Bi(III)/Fe(III) was added dropwise to the ammonium metavanadate mixture and sonicated for 15 min. Then, the as-prepared mixture was transferred to a Teflon-lined autoclave and allowed to the muffle furnace at 180 °C for 24 h. Finally, the acquired $\text{Bi}_{0.7}\text{Fe}_{0.3}\text{VO}_4$, $\text{Bi}_{0.5}\text{Fe}_{0.5}\text{VO}_4$, $\text{Bi}_{0.3}\text{Fe}_{0.7}\text{VO}_4$ photocatalysts were washed with deionized and ethyl alcohol several times and allowed to dry in a hot air oven at 80 °C overnight. The same procedure mentioned above has been followed to prepare pristine BiVO_4 and FeVO_4 without any molar fraction of other metal cations.

2.4. Synthesis of $\text{Bi}_x\text{Fe}_{1-x}\text{VO}_4/\text{SCN}$ nanocomposite

The $\text{Bi}_x\text{Fe}_{1-x}\text{VO}_4/\text{SCN}$ nanocomposite was synthesized by the total solvent evaporation technique. In brief, 0.1 g of SCN was dissolved in 40 mL methyl alcohol and bath sonicated for 30 min and followed by the addition of 0.1 g $\text{Bi}_x\text{Fe}_{1-x}\text{VO}_4$ ($x = 0.7, 0.5, 0.3$). The obtained mixture was then transferred to the hot magnetic stirrer and stirred at 50 °C until the methyl alcohol got total evaporation. Finally, the obtained $\text{Bi}_x\text{Fe}_{1-x}\text{VO}_4/\text{SCN}$ ($x = 0.7, 0.5, 0.3$) nanocomposites were allowed into a hot air oven at 80 °C overnight.

2.5. Photoelectrochemical (PEC) water-splitting and photocatalytic degradation measurements

Photoelectrochemical (PEC) measurements were carried out using as-synthesized CN, SCN, BiVO₄, FeVO₄, Bi_xFe_{1-x}VO₄, and Bi_xFe_{1-x}VO₄/

SCN ($x = 0.7, 0.5, 0.3$) samples coated ITO plates as photoanodes. In brief, 0.01 g of as-synthesized photocatalysts were dissolved in 2 mL of DI water-isopropyl alcohol mixture (3:1) followed by 0.01 mL of 5 wt% nafion-ethanol mixture and bath sonicated for 30 min. About 20 μ L of as-prepared homogenous mixtures were drop coated on pre-cleaned ITO plates ($1 \times 1 \text{ cm}^2$) and dried in a hot air oven at 50 $^\circ\text{C}$. The PEC water splitting reactions were performed on a CHI1211C (CH Instruments Inc.) electrochemical workstation using a standard three-electrode configuration system. The PEC water splitting, transient photocurrent, electrochemical impedance (EIS) measurements were conducted in the presence of specific 1.0 M Na_2SO_3 in 0.1 M potassium phosphate buffer (KPi, $\text{pH}=7.5$), 0.1 M NaOH, and 0.005 M $[\text{Fe}(\text{CN})_6]^{3-/4-}$ electrolytes, respectively. On the other hand, the photocatalytic degradation reactions were carried out using 100 mL of 50 mg L^{-1} roxarsone (ROX) dispersed with 50 mg of as-prepared different $\text{Bi}_x\text{Fe}_{1-x}\text{VO}_4/\text{SCN}$ photocatalysts. Then the above solution was stirred for 30 min before the light irradiation to accomplish catalyst-roxarsone (adsorption/desorption) equilibrium. For the photocatalysis reactions, simulated visible-light irradiation was given from the top of the photocatalytic reactor kept at a 40 cm distance. During the visible-light irradiation, about 3 mL of aliquots were taken every 5 minutes, filtered by 0.22 μm sterile syringe filters (PureTechTM, Taiwan), and used for further spectrophotometric measurements (Shimadzu UV-Vis spectrophotometer, UV-1800, Japan) for the confirmations of ROX degradation. For PEC measurements, the Ag/AgCl potential scale was converted to the reversible hydrogen electrode scale (RHE) using the below-mentioned equation (Eq. (1)).

$$E_{\text{RHE}} = E_{\text{Ag}/\text{AgCl}} + E_{\text{Ag}/\text{AgCl}}^0 + 0.0591 \times \text{pH} \quad (1)$$

where $E_{\text{Ag}/\text{AgCl}}^0 = 0.1976 \text{ V}$ at 25°C , $\text{pH} = \text{pH}$ of the electrolyte, $E_{\text{Ag}/\text{AgCl}}$ = experimental potential vs. Ag/AgCl reference electrode. The electrochemical active surface area (ECSA) of the as-prepared photoanodes were calculated from the equation of ($\text{ECSA} = R_f S$), in which R_f is the roughness factor, and S represents the geometric surface area of the photoanode (working electrode). The roughness factor leads to the relation of $R_f = C_{\text{dl}}/C_s$, where the electrochemical double-layer capacitance (C_{dl}) of the ideal smooth oxide surface (C_s) is $40 \mu\text{F cm}^{-2}$. The C_{dl} of the different photoanodes can be derived from the slope ($C_{\text{dl}} = \frac{1}{2}$ slope) of linear expression derived by plotting the Δj ($j_{\text{anodic}} - j_{\text{cathodic}}$) at 0.75 V (vs RHE) against the different scan rates.

3. Results and discussion

The crystal structures of as-synthesized photocatalysts were obtained by X-ray diffraction patterns shown in Fig. 1(A–C). The g-C₃N₄ (CN) shows two distinct XRD peaks located at 27.5° and 13.1° indexed to the (002) and (100) crystal planes (JCPDS No. 87-1526) arising because of interlayer stacking of aromatic systems (*d* = 0.326 nm) and in-plane structural packing of tri-s-triazine units (*d* = 0.6896 nm), respectively (Fig. 1A). Likewise, the SCN also depicts the same characteristic peaks, in which the major peak (27.7°) was slightly shifted to a larger 2θ value (0.161°) than the CN indicates that the decrease in the interlayer distance (*d* = 0.321 nm) (Fig. 1A inset). Thus, the appearance of two characteristic peaks of CN and SCN samples confirm that the basic graphitic structure remains unchanged. On the other hand, the widening of SCN peaks compared to the native CN is due to the lattice distortion and grain refinement effect by sulfur doping [30]. Fig. 1B depicts the XRD patterns of as-synthesized BiVO₄, and Bi_{0.7}Fe_{1-x}VO₄ (*x* = 0.7, 0.5, 0.3) specimens. The monoclinic BiVO₄ exhibits the main characteristic peaks appeared at 15.5°, 18.6°, 28.8°, 30.5°, 34.5°, 35.2°, 39.5°, 42.4°, 45.9°, 46.7°, 47.3°, 50.3°, 53.2°, 55.8°, 58.3°, 59.4°, 66.1°, 69.7°, 74.4°, and 76.5° are corresponding to the following (020), (011), (121), (040), (200), (002), (112), (150), (132), (240), (042), (202), (161), (251), (170), (321), (123), (127), (040), and (316) planes, respectively (JCPDS No. 14-0668) [31,32]. Moreover, the pristine triclinic FeVO₄ (Fig. S1) shows the following XRD peaks at 16.6°, 21.2°, 25.0°, 28.4°, 32.1°,

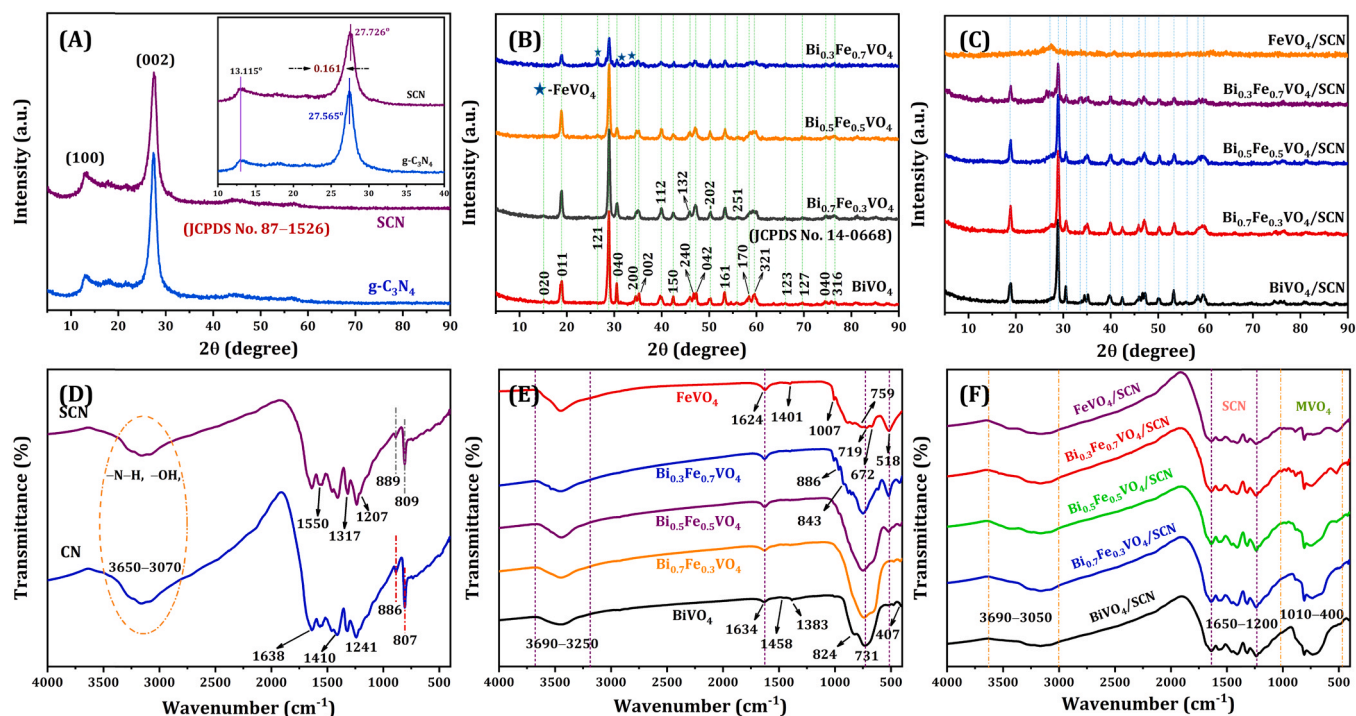


Fig. 1. X-ray diffraction patterns and Fourier-transform infrared spectra of as-prepared CN, and SCN (A and D), BiVO_4 , $\text{Bi}_x\text{Fe}_{1-x}\text{VO}_4$ ($x = 0.7, 0.5, 0.3$), and FeVO_4 (B and E), BiVO_4/SCN , $\text{Bi}_x\text{Fe}_{1-x}\text{VO}_4/\text{SCN}$ ($x = 0.7, 0.5, 0.3$), and FeVO_4/SCN (C and F).

34.2° , and 41.8° , which are attributed to the (110), (111), (120), (220), (221), (300), and (330) planes (JCPDS No. 38–1372) [33]. For the various $\text{Bi}_x\text{Fe}_{1-x}\text{VO}_4$ ($x = 0.7, 0.5, 0.3$) samples, the FeVO_4 peaks (\star) were observed from $\text{Bi}_{0.5}\text{Fe}_{0.5}\text{VO}_4$ to $\text{Bi}_{0.3}\text{Fe}_{0.7}\text{VO}_4$, and no other FeVO_4 peaks are observed in $\text{Bi}_{0.7}\text{Fe}_{0.3}\text{VO}_4$ owing to its low content, but the peak intensities of BiVO_4 were changed concerning its content (mixed-phase) [34]. Besides, the XRD patterns of BiVO_4/SCN , $\text{Bi}_x\text{Fe}_{1-x}\text{VO}_4/\text{SCN}$ ($x = 0.7, 0.5, 0.3$), and FeVO_4/SCN nanocomposites were shown in Fig. 1C. However, it confirms the successive impregnation of BiVO_4 , FeVO_4 , and $\text{Bi}_x\text{Fe}_{1-x}\text{VO}_4$ on SCN by the presence of their combined characteristic XRD patterns.

The FT-IR spectra were recorded in the range of $4000\text{--}400\text{ cm}^{-1}$ to analyze the different chemical bonds and functional groups present in CN, SCN, BiVO_4 , $\text{Bi}_x\text{Fe}_{1-x}\text{VO}_4$ ($x = 0.7, 0.5, 0.3$), FeVO_4 , BiVO_4/SCN , $\text{Bi}_x\text{Fe}_{1-x}\text{VO}_4/\text{SCN}$, and FeVO_4/SCN (Fig. 1D–F). As seen in Fig. 1D, the FT-IR spectra of CN and SCN show two distinctive sharp peaks that appeared at 807 and 886 cm^{-1} are attributed to the stretching vibration modes of tri-s-triazine units (C--N--C), and deformation of N--H [35] respectively. The characteristic bands that appeared in the range of $1650\text{--}1200\text{ cm}^{-1}$ are ascribed to the typical stretching vibration modes of aromatic N--C=N , ($\text{C}_3\text{--N}$) groups present in the heterocycle rings of CN. A comprehensive vibrational band located at $3690\text{--}3050\text{ cm}^{-1}$ region can be ascribed to the stretching vibration modes of --N--H , =N--H associated with the uncondensed free amine groups, and --OH by the physically absorbed surface water molecules. The FT-IR spectrum of BiVO_4 illustrates the following specific bands at $407, 731, 823\text{ cm}^{-1}$ are attributed to the symmetric bending, asymmetric, and symmetric stretching vibrations of VO_4^{3-} , respectively [36]. Meanwhile, the FeVO_4 exhibits the vibration bands at $517, 672$, and 718 cm^{-1} , representing the Fe--O stretching/ V--O--V deformation and bridging V--O--Fe modes, respectively [37]. Also, the following vibration bands that appeared at $886, 1007\text{ cm}^{-1}$ are associated with the terminal V--O stretching vibration modes. BiVO_4 and FeVO_4 show two bands at 1634 and 3446 cm^{-1} corresponding to the O--H stretching vibrations due to the adsorbed water molecules. The FT-IR spectra of $\text{Bi}_x\text{Fe}_{1-x}\text{VO}_4$ ($x = 0.7, 0.5, 0.3$) demonstrate the combined peak composition of BiVO_4 and FeVO_4 and

agree with the XRD results (Fig. 1E). As seen in Fig. 1F, the FT-IR spectra of BiVO_4/SCN , $\text{Bi}_x\text{Fe}_{1-x}\text{VO}_4/\text{SCN}$ ($x = 0.7, 0.5, 0.3$), and FeVO_4/SCN nanocomposites revealed the occurrence of integrated vibrational bands of BiVO_4 , FeVO_4 , and SCN, which endorses the successive impregnation and chemical interactions.

The optical absorbance spectra and apparent bandgap energies (E_g) of the as-prepared CN, SCN, BiVO_4 , FeVO_4 , $\text{Bi}_x\text{Fe}_{1-x}\text{VO}_4$, and $\text{Bi}_x\text{Fe}_{1-x}\text{VO}_4/\text{SCN}$ ($x = 0.7, 0.5, 0.3$) photocatalysts were analyzed by UV–Vis diffuse reflectance spectroscopy (UV–Vis DRS), and Tauc analysis respectively. As seen in Fig. 2A, the absorbance band edge of SCN ($\sim 469\text{ nm}$) is extended than CN ($\sim 457\text{ nm}$). The absorption band tail extension in SCN may correspond to a slight fraction of a conducting phase. The S doping leads to the formation of occupied C1-p_z states at the CB level, which results in the CN material being a conductor. Indeed, this transformation is not favorable for photocatalytic activities. However, owing to the assumption that sulfur is not distributed uniformly over the CN, the un-doped part will act as an anode. In the meantime, the S doped conducting portion will serve as a co-catalyst and collects the photogenerated electrons. At the same time, BiVO_4 and FeVO_4 exhibited band edge values of ~ 510 and $\sim 639\text{ nm}$, respectively. Meanwhile, the $\text{Bi}_x\text{Fe}_{1-x}\text{VO}_4$ ($x = 0.7, 0.5, 0.3$) unveils the optical band edge values ($\sim 530, \sim 541$, and $\sim 566\text{ nm}$) according to the apparent color changes (insets of Fig. 2A and C) from yellow (BiVO_4) to brown (FeVO_4) concerning the Bi and Fe contents. Also, the enhanced absorbance band edge values of BiVO_4/SCN ($\sim 508\text{ nm}$), $\text{Bi}_{0.7}\text{Fe}_{0.3}\text{VO}_4/\text{SCN}$ (~ 521), $\text{Bi}_{0.5}\text{Fe}_{0.5}\text{VO}_4/\text{SCN}$ (~ 532), $\text{Bi}_{0.3}\text{Fe}_{0.7}\text{VO}_4/\text{SCN}$ (~ 569), and FeVO_4/SCN ($\sim 623\text{ nm}$) are owing to the synergistic effect of combined SCN and $\text{Bi}_x\text{Fe}_{1-x}\text{VO}_4$, which is beneficial to the enhanced photocatalytic activities with reduced recombination effect (Fig. 2C). In addition, the optical bandgap energies of the samples were calculated by Tauc plots using Kubelka-Munk function ($\alpha h\nu = A(h\nu - E_g)^n$) [38]. As seen in Fig. 2B, the optical bandgap values of the CN, SCN, BiVO_4 , $\text{Bi}_{0.7}\text{Fe}_{0.3}\text{VO}_4/\text{SCN}$, $\text{Bi}_{0.5}\text{Fe}_{0.5}\text{VO}_4/\text{SCN}$, $\text{Bi}_{0.3}\text{Fe}_{0.7}\text{VO}_4/\text{SCN}$, and FeVO_4 photocatalysts were calculated to be $2.71, 2.64, 2.43, 2.34, 2.29, 2.19$, and 1.94 eV , respectively. On the other hand, the bandgap energies of BiVO_4/SCN , $\text{Bi}_{0.7}\text{Fe}_{0.3}\text{VO}_4/\text{SCN}$, $\text{Bi}_{0.5}\text{Fe}_{0.5}\text{VO}_4/\text{SCN}$, $\text{Bi}_{0.3}\text{Fe}_{0.7}\text{VO}_4/\text{SCN}$,

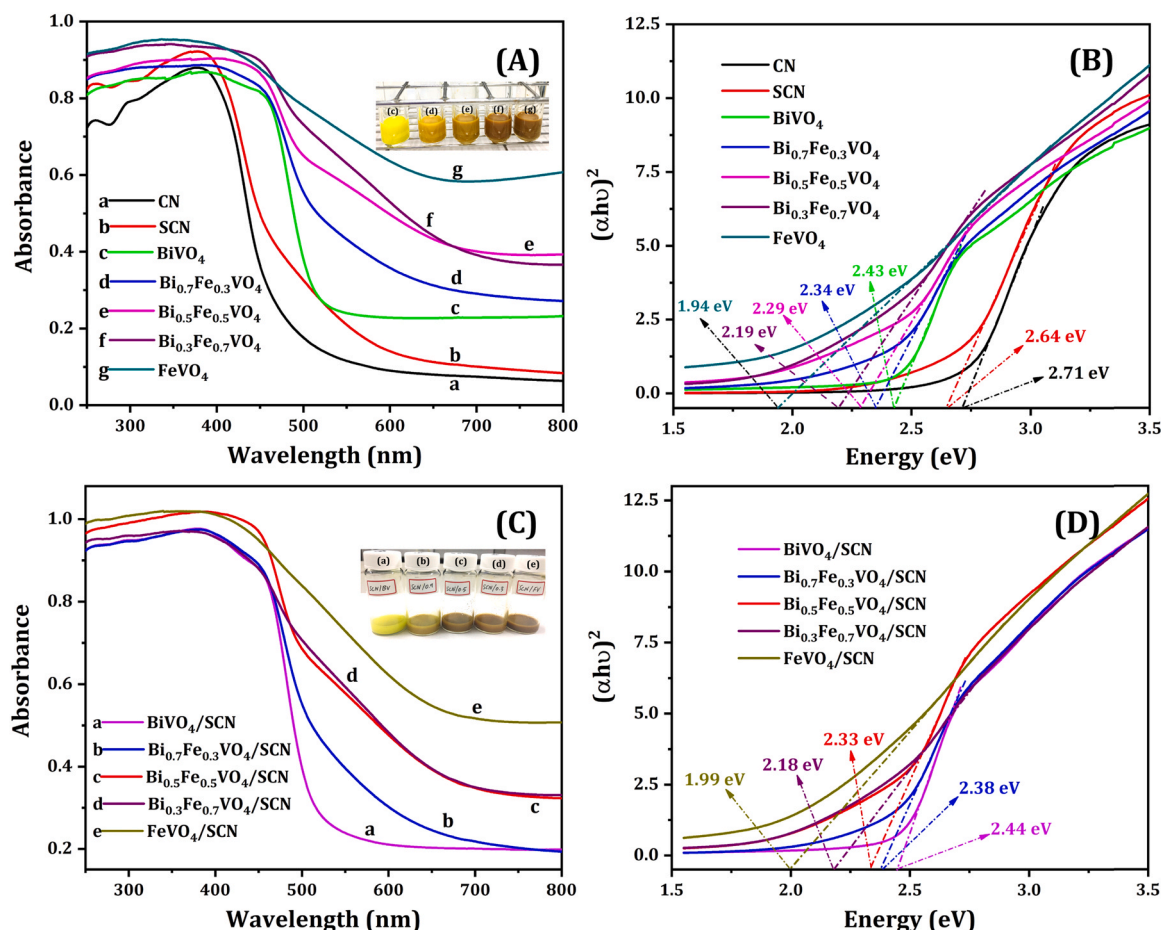


Fig. 2. UV-Vis diffuse reflectance spectra of as-prepared CN, SCN, BiVO₄, FeVO₄, and Bi_xFe_{1-x}VO₄ (x = 0.7, 0.5, 0.3) samples (A and C), the digital photographs of the Bi_xFe_{1-x}VO₄ (A-inset) Bi_xFe_{1-x}VO₄/SCN (C-inset) sample solutions, and their corresponding Tauc plots (B and D).

and FeVO₄/SCN are found to be 2.44, 2.38, 2.33, 2.18, and 1.99 eV, respectively (Fig. 2D). Therefore, the above results suggest that adding of Fe content to the BiVO₄ leads to enhanced light-harvesting (> 520 nm), and integration with SCN reduces the recombination rate of photogenerated charge carriers and superior photocatalytic efficiency.

In addition, the photoexcitation of electrons and the recombination rate of charge carriers of the synthesized photocatalysts were measured by photoluminescence (PL) spectroscopy (Fig. S2). The PL studies were conducted using 266 nm exciting radiation in the wavelength range of (350–900 nm) at standard ambient temperature (~ 24 °C). The PL intensity is directly proportional to the recombination rate of photo-generated charge carriers (i.e. electrons and holes). Thus the observed PL intensity of SCN is much lower than CN indicates the suppressed recombination rate. As seen in Fig. S2 inset, the magnified PL spectra of BiVO₄, FeVO₄, and Bi_xFe_{1-x}VO₄, and BiVO₄/SCN, FeVO₄/SCN, Bi_xFe_{1-x}VO₄/SCN (x = 0.7, 0.5, 0.3) intensely exhibits that the fastest recombination rate of BiVO₄, FeVO₄, Bi_xFe_{1-x}VO₄ mixed vanadate materials are quietly reduced by the synergistic effect of SCN formed by the different heterojunctions. Hence, the increased lifetime of photo-generated charge carriers and suppressed electron-hole recombination facilitates the enrichment in the photocatalytic performances.

The heterostructure formation and surface morphologies of CN, SCN, BiVO₄, Bi_xFe_{1-x}VO₄ (x = 0.7, 0.5, 0.3), FeVO₄ (Fig. 3A–G), BiVO₄/SCN, Bi_xFe_{1-x}VO₄/SCN (x = 0.7, 0.5, 0.3), and FeVO₄/SCN (Fig. 3G–L) samples were analyzed by field-emission scanning electron microscopy (FE-SEM). Both CN and SCN exhibits similar graphitic-like morphologies, and there is no obvious change observed (Fig. 3A–B). Also, these stacked lamellar sheet-like structures facilitate a host surface to impregnate the

Bi_xFe_{1-x}VO₄ heterostructures. Besides, the pristine monoclinic BiVO₄ has a dendritic-like morphology (Fig. 3C), whereas the pristine triclinic FeVO₄ has an ultrathin nanosheet-like morphology (Fig. 3G). The FESEM images of Bi_{0.7}Fe_{0.3}VO₄, Bi_{0.5}Fe_{0.5}VO₄, and Bi_{0.3}Fe_{0.7}VO₄ are presented in Fig. 3D–F. When compared to the (x = 0.7) and (x = 0.3), the equal stoichiometric (x = 0.5) exhibits a sphere-like morphology arranged by the accumulation of Bi_{0.5}Fe_{0.5}VO₄ nanoplates. Also, their corresponding BiVO₄/SCN, Bi_xFe_{1-x}VO₄/SCN (x = 0.7, 0.5, 0.3), and FeVO₄/SCN nanocomposites shows the successful impregnation of MVO₄ on the surface of SCN are demonstrated in Fig. 3H–L.

The elemental mapping images shown in Fig. 4A–E confirms the occurrence and homogeneous distribution of the different elements (Bi, Fe, V, and O) existing throughout the Bi_{0.5}Fe_{0.5}VO₄ sample. On the other hand, the existence and quantities of C, N, O, S, V, Fe, and Bi elements occurred in SCN (Fig. 5A), BiVO₄ (Fig. 5B), FeVO₄ (Fig. 5C), Bi_xFe_{1-x}VO₄ (x = 0.7, 0.5, 0.3) (Fig. 5D–F), and Bi_xFe_{1-x}VO₄/SCN (x = 0.7, 0.5, 0.3) (Fig. 5G–I) nanocomposites were evaluated by energy-dispersive X-ray (EDX) spectroscopy analysis. The EDX spectra of Bi_xFe_{1-x}VO₄ (x = 0.7, 0.5, 0.3) (Fig. 5D–F) clearly indicates that the elemental ratio of Bi and Fe follows the amount of precursor added. Owing to the smaller percentage of S, the EDX spectra of Bi_xFe_{1-x}VO₄/SCN (x = 0.7, 0.5, 0.3) (Fig. 5G–I) cannot detect any peaks associated with sulfur. Therefore, the EDX analysis confirms the presence and the purity of as-synthesized different photocatalysts.

The surface chemical environment and the elemental composition of the synthesized photocatalytic materials were confirmed by X-ray photoelectron spectroscopy (XPS). The XPS survey spectra of CN, SCN, BiVO₄, Bi_xFe_{1-x}VO₄/SCN (x = 0.7, 0.5, 0.3), and FeVO₄ samples were

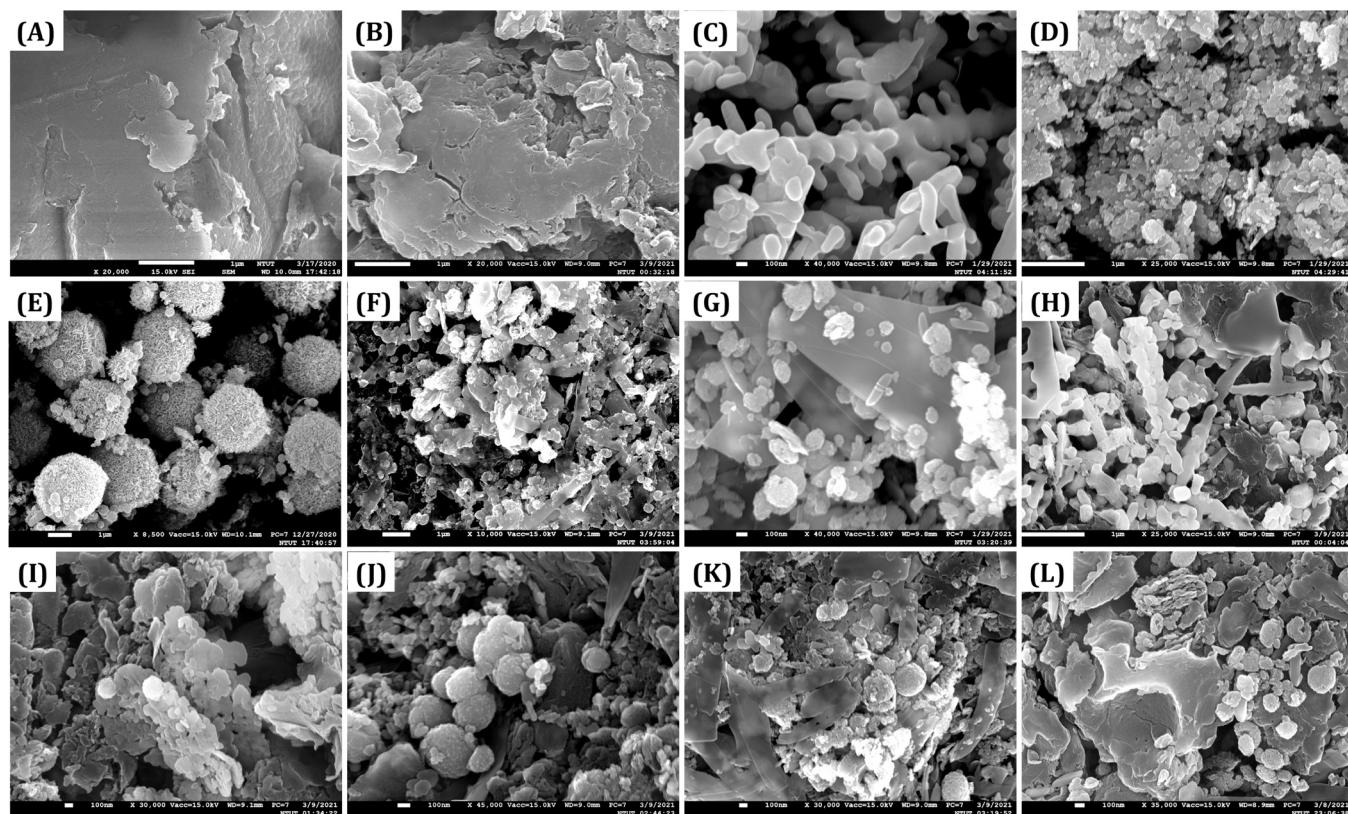


Fig. 3. The FE-SEM images of CN (A), SCN (B), BiVO_4 (C), $\text{Bi}_{0.7}\text{Fe}_{0.3}\text{VO}_4$ (D), $\text{Bi}_{0.5}\text{Fe}_{0.5}\text{VO}_4$ (E), $\text{Bi}_{0.3}\text{Fe}_{0.7}\text{VO}_4$ (F), FeVO_4 (G), BiVO_4/SCN (H), $\text{Bi}_{0.7}\text{Fe}_{0.3}\text{VO}_4/\text{SCN}$ (I), $\text{Bi}_{0.5}\text{Fe}_{0.5}\text{VO}_4/\text{SCN}$ (J), $\text{Bi}_{0.3}\text{Fe}_{0.7}\text{VO}_4/\text{SCN}$ (K), and FeVO_4/SCN (L).

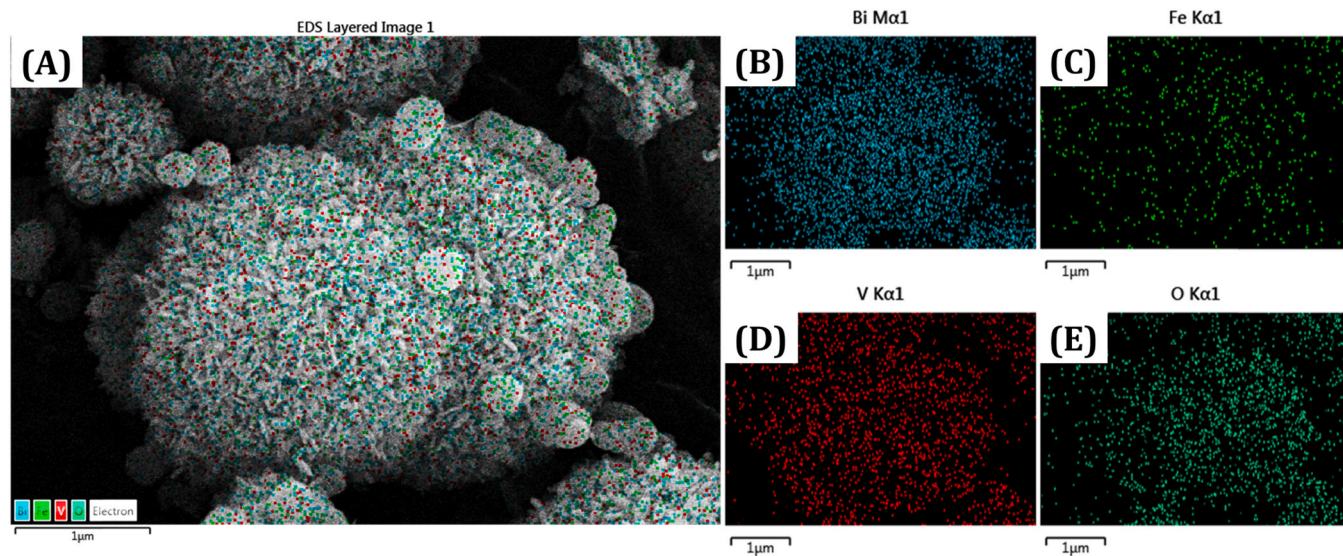


Fig. 4. The mapping image of $\text{Bi}_{0.5}\text{Fe}_{0.5}\text{VO}_4$ sample (A), Bi (B), Fe (C), V (D), and O (E).

obtained in the binding energy range of (0–1200 eV) shown in Fig. 6A, and which are revealed the occurrence of corresponding C1s, N1s, S2p, Bi4f, Fe2p, V2p, O 1s elements in their surfaces. All of the obtained XPS spectra were corrected concerning the adventitious carbon peak (284.6 eV). Fig. 6B–C shows the core-level XPS spectra of C1s and N1s obtained from SCN and $\text{Bi}_x\text{Fe}_{1-x}\text{VO}_4/\text{SCN}$ ($x = 0.7, 0.5, 0.3$) specimens. The XPS high-resolution spectra of C1s can be deconvoluted into three individual peaks positioned at 284.66, 287.29, and 289.13 eV, which can be ascribed to the adventitious carbon (C–C) present on the surface,

sp^2 hybridized C–N=C, and C–(N)₃ present in the heptazine ring structure, respectively [29]. As well, the deconvoluted high-resolution spectra of N 1s shows two distinct peaks centered at 399.63 and 401.38 eV corresponding to the N–(C)₃ and terminal amino (C–NH) groups, respectively [38]. The binding energies of C1s and N1s of $\text{Bi}_x\text{Fe}_{1-x}\text{VO}_4/\text{SCN}$ ($x = 0.7, 0.5, 0.3$) samples were shifted towards lower binding energies by (~ 0.53 eV) and (~ 0.78 eV) respectively, than pristine SCN. Thus, the shift to lower binding energy-reduced electron cloud on SCN surface due to the photogenerated electron relocation

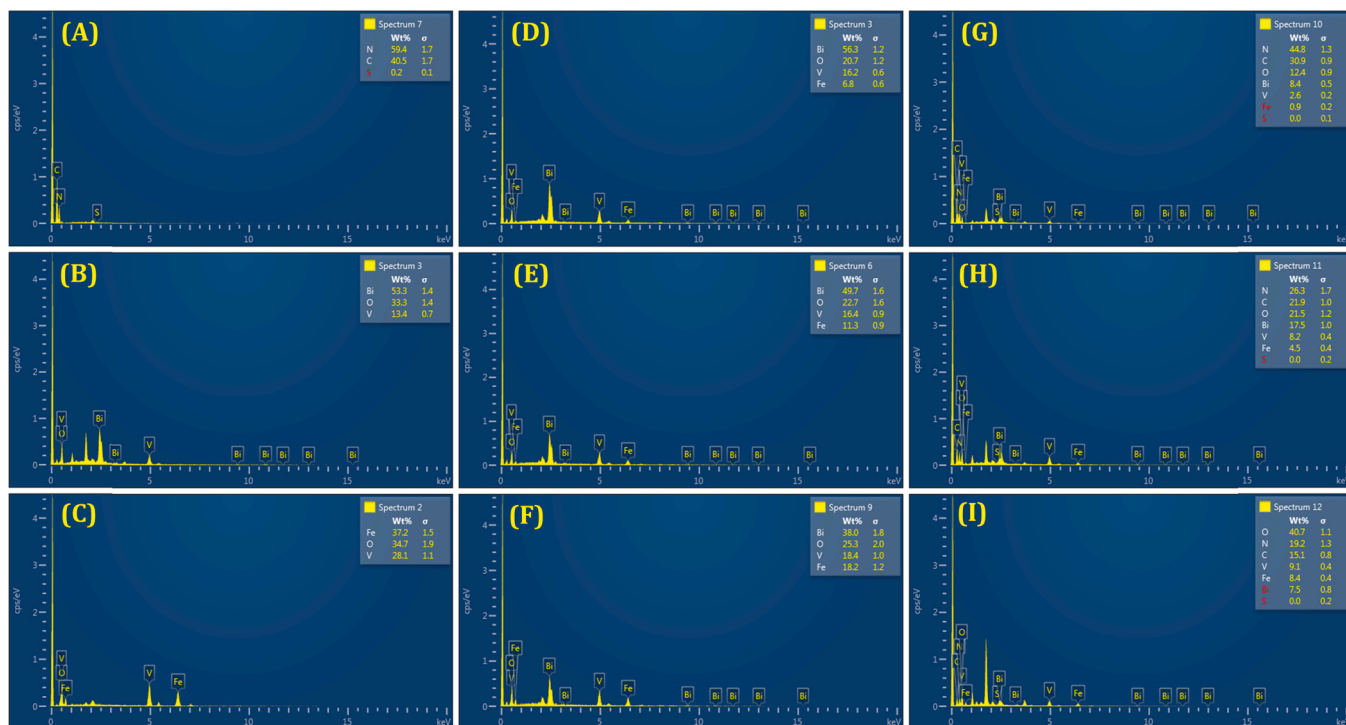


Fig. 5. The EDX elemental spectra of SCN (A), BiVO₄ (B), FeVO₄ (C), Bi_{0.7}Fe_{0.3}VO₄ (D), Bi_{0.5}Fe_{0.5}VO₄ (E), Bi_{0.3}Fe_{0.7}VO₄ (F), Bi_{0.7}Fe_{0.3}VO₄/SCN (G), Bi_{0.5}Fe_{0.5}VO₄/SCN (H), Bi_{0.3}Fe_{0.7}VO₄/SCN (I).

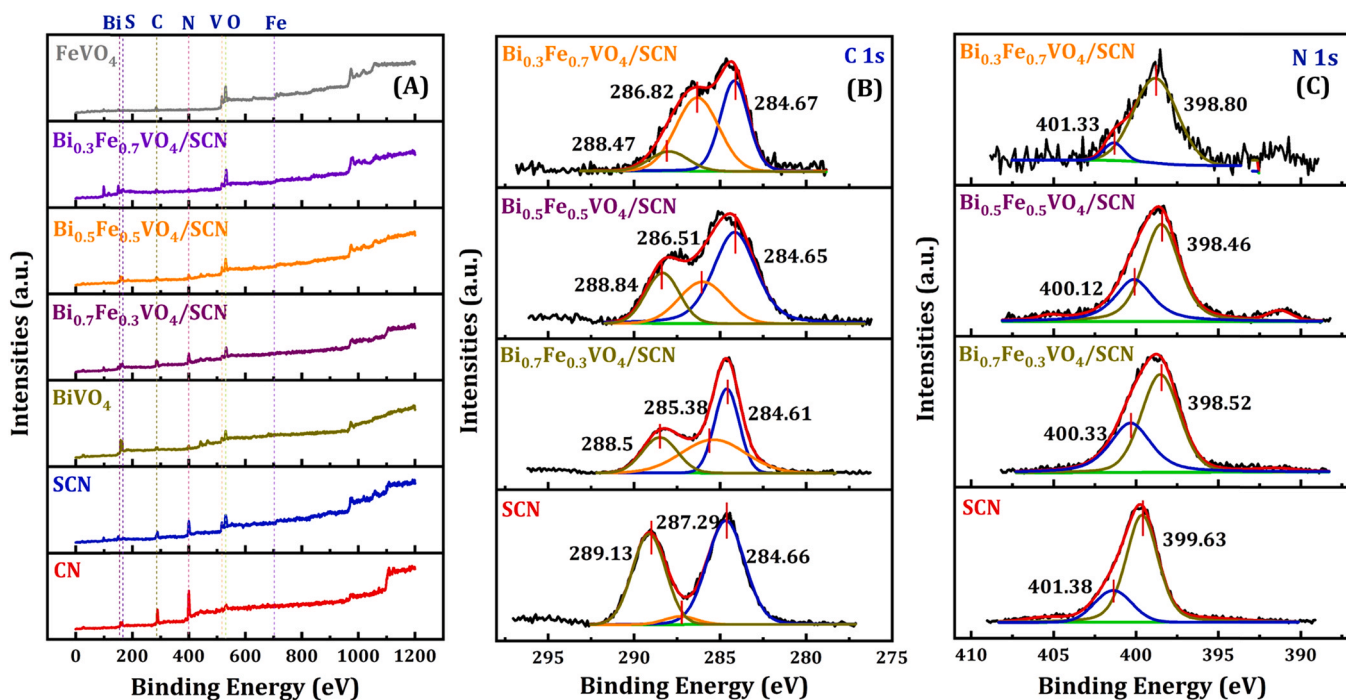


Fig. 6. The XPS survey spectra CN, SCN, BiVO₄, Bi_xFe_{1-x}VO₄/SCN ($x = 0.7, 0.5, 0.3$), and FeVO₄ (A), and high-resolution spectra of C 1s (B), N 1s (C).

from the CB of SCN to the CB of Bi_xFe_{1-x}VO₄ heterostructure.

The Bi4f core-level XPS spectra of pristine BiVO₄ (Fig. 7A) consists of two individual peaks positioned at 158.77 and 164.08 eV attributed to the Bi4f_{7/2} and Bi4f_{5/2} states, respectively [39]. Similarly, the Fe2p XPS high-resolution spectra of pristine FeVO₄ represent two peaks at binding energies of 710.47, and 724.68 eV are corresponding to the Fe2p_{3/2} and Fe2p_{1/2} peaks, respectively (Fig. 7B) [40]. The V2p high-resolution

spectra obtained from the samples show two distinctive peaks and can be ascribed to the V2p_{3/2} and V2p_{1/2} states. The V2p_{3/2} and V2p_{1/2} peaks of V2p for pristine BiVO₄ and FeVO₄ have appeared at 516.54, 523.84 eV, and 516.50, 523.94 eV, respectively (Fig. 7C) [39,40]. The core-level O1s spectra of the pristine samples can be deconvoluted into two peaks and can be endorsed to the lattice and dangling oxygen. In the meantime, the O1s core-level XPS peaks of BiVO₄ and FeVO₄ appear at

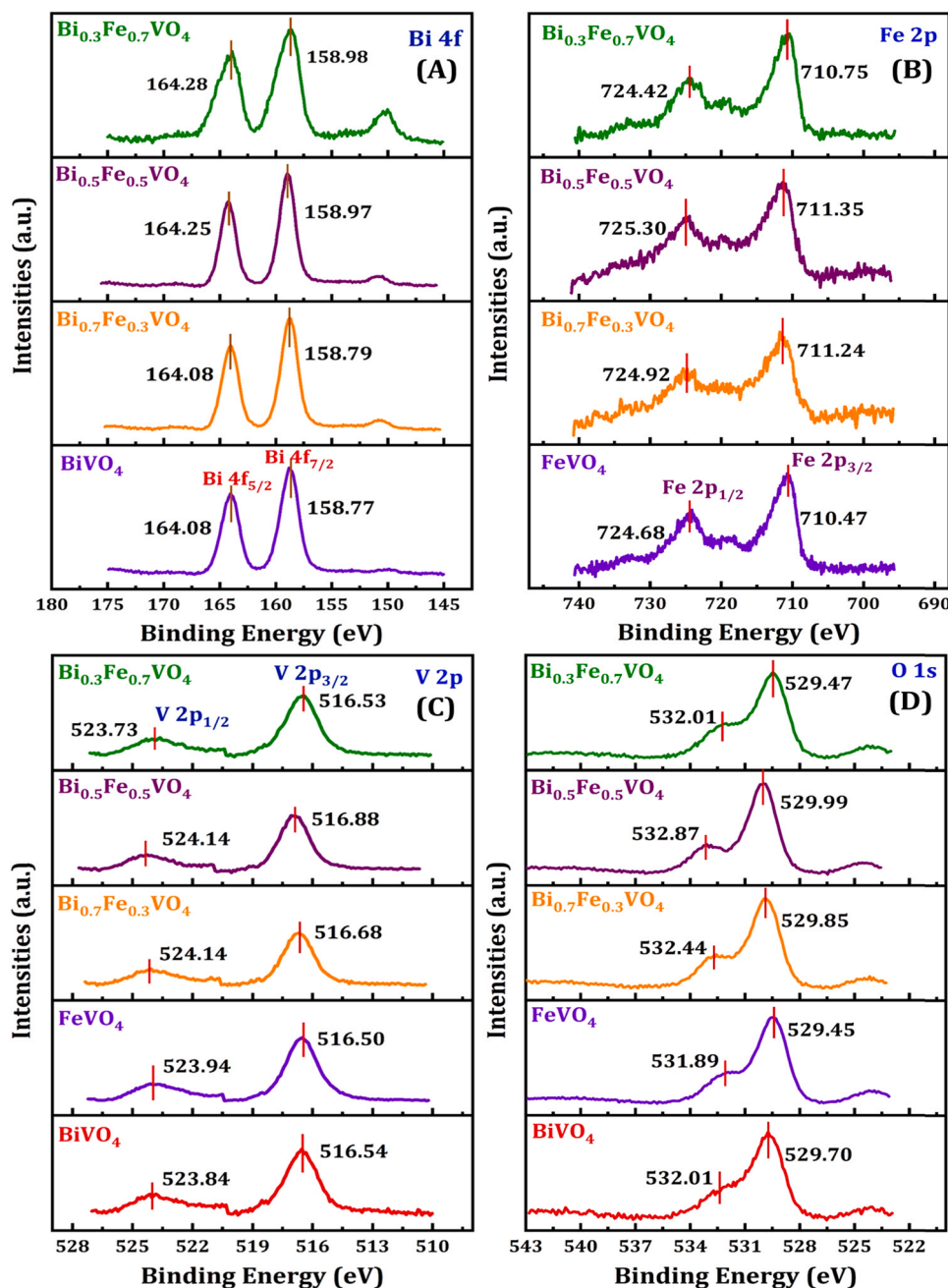


Fig. 7. The XPS high-resolution spectra of Bi4f (A), Fe2p (B), V2p (C), and O1s (D) were obtained from pristine BiVO_4 , FeVO_4 , and $\text{Bi}_x\text{Fe}_{1-x}\text{VO}_4$ ($x = 0.7, 0.5, 0.3$) samples.

529.70 and 529.45 eV, respectively (Fig. 7D). According to the order of electronegativity of the elements ($\text{O} > \text{Fe} > \text{V} > \text{Bi}$) and their contents, the binding energies of Bi4f (~ 0.12 eV), Fe2p (~ 0.2 eV), V2p (~ 0.11 eV), and O1s (~ 0.2 eV) present in the $\text{Bi}_x\text{Fe}_{1-x}\text{VO}_4$ ($x = 0.7, 0.5, 0.3$) samples were shifted to higher binding energies compared to the pristine samples.

Fig. S3A–D represents the XPS core-level spectra of Bi4f, Fe2p, V2p, and O1s acquired from the $\text{Bi}_x\text{Fe}_{1-x}\text{VO}_4/\text{SCN}$ ($x = 0.7, 0.5, 0.3$) nanocomposites, respectively. The high-resolution spectra of Bi4f, Fe2p, V2p, and O1s obtained from $\text{Bi}_x\text{Fe}_{1-x}\text{VO}_4/\text{SCN}$ ($x = 0.7, 0.5, 0.3$) nanocomposites are shifted towards lower binding energies when compared to the unmodified pristine samples. Compared with the pristine V2p peaks of BiVO_4 , FeVO_4 , and $\text{Bi}_x\text{Fe}_{1-x}\text{VO}_4$, the new peaks appeared at 517.75 eV 515.60 eV for the high-resolution XPS spectra of V2p of $\text{Bi}_x\text{Fe}_{1-x}\text{VO}_4/\text{SCN}$ indicates the V^{5+} state, while the peak at 521.84 eV

indicates the V^{3+} oxidation states of vanadium. Similarly, due to more electron clouds on the surface of $\text{Bi}_x\text{Fe}_{1-x}\text{VO}_4$, these peaks shift to higher binding energies. Therefore, the chemical shift has proved that electrons are transformed from CB of SCN to CB of $\text{Bi}_x\text{Fe}_{1-x}\text{VO}_4$ heterostructure, and a type-I & II heterojunctions are formed between SCN and $\text{Bi}_x\text{Fe}_{1-x}\text{VO}_4$. Among two types of heterojunctions, the type-II heterojunction facilitates the high separation and migration of photogenerated charge carriers between semiconductor-I and semiconductor-II. Therefore, the extended lifetime of the charge carriers will increase the efficiency of the photocatalytic reaction and the PEC oxygen evolution reaction. The atomic percentages of the elements present in the as-synthesized CN, SCN, BiVO_4 , $\text{Bi}_x\text{Fe}_{1-x}\text{VO}_4$, and FeVO_4 are tabulated as Table 1 concerning the peak area obtained by XPS spectroscopy.

Table 1

Atomic percentages of different elements were calculated by X-ray photoelectron spectroscopy with respect to their peak areas.

Samples	Elements (at%)						
	C	N	S	Bi	Fe	V	O
CN	43.46	56.54	–				
SCN	44.56	40.98	14.46				
BiVO ₄				16.98	–	16.43	66.58
Bi _{0.3} Fe _{0.7} VO ₄				5.13	11.96	17.05	65.84
Bi _{0.5} Fe _{0.5} VO ₄				12.74	11.53	13.82	61.90
Bi _{0.7} Fe _{0.3} VO ₄				15.29	8.44	14.09	62.55
FeVO ₄				–	12.28	20.17	67.54

3.1. Photoelectrochemical (PEC) measurements

The photoexcited charge transfer kinetics at the semiconductor-electrolyte is a significant factor for water-oxidation reactions and is measured by electrochemical impedance spectroscopic analysis (EIS). The different radius of semicircles found in the Nyquist plots reflects the overall resistance of the corresponding semiconductor material and nanocomposites. Also, the charge transfer resistance (R_{ct}) measures the transportation of photogenerated electrons and holes from the semiconductor surface to the electrolyte, which has been considered the rate-determining step in water-oxidation reactions. The Nyquist plots of CN, SCN, BiVO₄, Bi_xFe_{1-x}VO₄, FeVO₄, BiVO₄/SCN, Bi_xFe_{1-x}VO₄/SCN ($x = 0.7, 0.5, 0.3$), and FeVO₄/SCN derived by EIS analysis were shown in Fig. 8A and C. The R_{ct} values of the CN, SCN, BiVO₄, Bi_{0.7}Fe_{0.3}VO₄, Bi_{0.5}Fe_{0.5}VO₄, Bi_{0.3}Fe_{0.7}VO₄, and FeVO₄ are calculated to be 15.0 Ω , 10.6 Ω , 32.7 Ω , 36.7 Ω , 31.8 Ω , 39.5 Ω , and 25.1 Ω respectively. Similarly, The R_{ct} values of the BiVO₄/SCN, Bi_{0.7}Fe_{0.3}VO₄/SCN, Bi_{0.5}Fe_{0.5}VO₄/SCN, Bi_{0.3}Fe_{0.7}VO₄/SCN, and FeVO₄/SCN are calculated to be 44.9 Ω , 21.9 Ω , 21.7 Ω , 47.8 Ω , and 33.9 Ω respectively. It is clear that the SCN has a lower resistance than the CN due to the sulfur effect.

On the other hand, Bi_{0.5}Fe_{0.5}VO₄ and Bi_{0.5}Fe_{0.5}VO₄/SCN have the least R_{ct} values than other samples. The radius of the semicircle either increased or decreased with respect to the change in the ratio of Bi and Fe. Among various proportions, ($X = 0.5$) exhibits the excellent carrier transferability, suggesting tremendous charge separation and enhanced photoelectrochemical performances. In addition, the equivalent circuit diagrams of the EIS-Nyquist plots were given as the insets of Fig. 8A and C, and where, R_s = electrolyte or solution resistance; C_{dl} = double layer capacitance; R_{ct} = charge transfer resistance; Z_w = Warburg impedance (diffusion).

Furthermore, the transient photocurrent responses of the prepared photocatalysts were investigated to confirm the photogenerated charge separation efficiency and the lifespan of photoexcited charge carriers. The photocurrent analysis was performed in the presence of 0.1M NaOH at an operating potential of 1.2 V (vs RHE) under visible-light irradiation with On/Off conditions. It can be seen from Fig. 8B, the photocurrent density of SCN (6.85 μ A) is 2.1 folds higher than the CN (3.22 μ A), and lower photocurrent densities ($\sim 0.603 \pm 0.05 \mu$ A) were obtained for BiVO₄, Bi_xFe_{1-x}VO₄ ($x = 0.7, 0.5, 0.3$), FeVO₄ pristine samples due to their poor charge separation efficiency and fast electron-hole recombination rates. In contrast, BiVO₄/SCN, Bi_xFe_{1-x}VO₄/SCN ($x = 0.7, 0.5, 0.3$), FeVO₄/SCN nanocomposites unveil the enhanced photogenerated charge carrier separation and lifetime. Thus, the photocurrent densities of BiVO₄/SCN (3.79 μ A) and FeVO₄/SCN (1.52 μ A) are 2.9 and 6.0 folds higher than that of pristine BiVO₄ (1.31 μ A) and FeVO₄ (0.25 μ A), respectively. The apparent photocurrent density of Bi_{0.5}Fe_{0.5}VO₄ (6.75 μ A) significantly higher (i.e. 3.8, 2.7, 2.6, and 4.4 folds) than that of BiVO₄/SCN (1.78 μ A), Bi_{0.7}Fe_{0.3}VO₄/SCN (2.42 μ A), Bi_{0.3}Fe_{0.7}VO₄/SCN (2.61 μ A), and FeVO₄/SCN (1.52 μ A), respectively (Fig. 8D). The Bi_{0.5}Fe_{0.5}VO₄ exhibits a photocurrent peak with a different shape than the Bi_{0.7}Fe_{0.3}VO₄ due to the high charge accumulation during the light illumination. We can also see the same kind of photocurrent peak for the Bi_{0.3}Fe_{0.7}VO₄. This result also

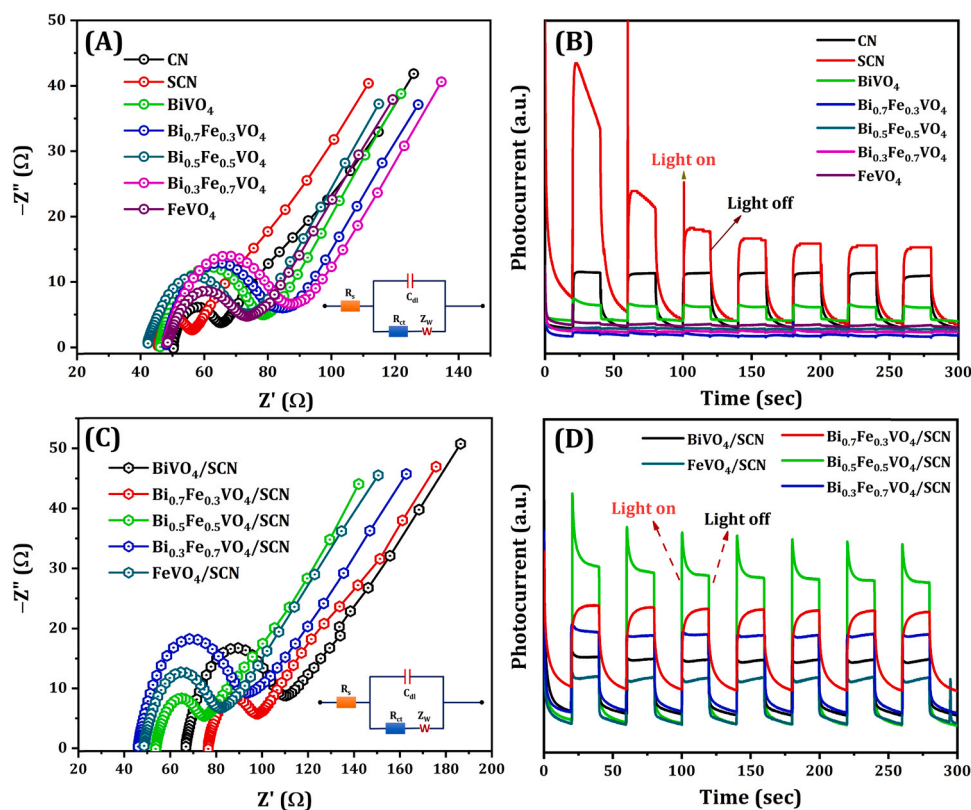


Fig. 8. The EIS Nyquist plots (A and C) and amperometric photocurrent ($i-t$) curves (B and D) of CN, SCN, BiVO₄, Bi_xFe_{1-x}VO₄, FeVO₄, and BiVO₄/SCN, Bi_xFe_{1-x}VO₄/SCN ($x = 0.7, 0.5, 0.3$), and FeVO₄/SCN.

demonstrates the amount of Fe influences the high charge accumulation during light irradiation [41]. As observed from these results, the heterostructure formation between SCN and $\text{Bi}_x\text{Fe}_{1-x}\text{VO}_4$ could make the charge transport through the type-II heterojunction pathway, and the effective separation of charge carriers from recombination leads to an increase in photocurrent density as well as photoelectrochemical efficiency.

The electrochemical properties of the semiconductor materials were characterized by Mott-Schottky (M-S) analysis in the presence of 0.1 M Na_2SO_4 as a supporting electrolyte under dark conditions. The slope and the intercept at the x-axis acquired by the M-S curve determines a donor density (N_D) available for the photoelectrochemical reactions and flat-band potential (V_{FB}) of the semiconductor-electrolyte interface, respectively. The Mott-Schottky plots obtained for all the photoanodes indicating the n-type nature of SCN, BiVO_4 , $\text{Bi}_x\text{Fe}_{1-x}\text{VO}_4$ ($x = 0.7, 0.5, 0.3$), FeVO_4 , BiVO_4/SCN , $\text{Bi}_x\text{Fe}_{1-x}\text{VO}_4/\text{SCN}$ ($x = 0.7, 0.5, 0.3$), and FeVO_4/SCN (Fig. 9A–C). The relationship between capacitance and voltage across the semiconductor/electrolyte interface can be obtained by the following Mott-Schottky equation (Eq. (2)) [42,43],

$$\frac{1}{C^2} = \left(\frac{2}{A^2 \epsilon_0 \epsilon \epsilon_0 N_D} \right) \left[V - \left(V_{\text{FB}} + \frac{k_B T}{e_0} \right) \right] \quad (2)$$

where C is the capacitance at space charge layer, A =working electrode area (1 cm^2), ϵ = dielectric constant, ϵ_0 = permittivity of free space ($\epsilon_0 = 8.854 \times 10^{-12} \text{ F m}^{-1}$), N_D =carrier density, V = applied bias, V_{FB} = flat-band potential, k_B = Boltzmann constant ($k_B = 1.380 \times 10^{-23} \text{ m}^2 \text{ kg s}^{-2} \text{ K}^{-1}$), T = absolute temperature ($T = 298 \text{ K}$), and e_0 = charge of electron ($e_0 = 1.60 \times 10^{-19} \text{ C}$). The value of $(V_{\text{FB}} + k_B T/e_0)$ can be derived for the intercept at the potential axis by the extrapolation of $1/C^2$ to zero. Also, from the slope value of the Mott-Schottky plot, the donor density (N_D) can be calculated by the below-mentioned equations (Eq. (3)),

$$N_D = \left(\frac{2}{A^2 \epsilon_0 \epsilon \epsilon_0} \right) \times \left[\frac{d \left(\frac{1}{C^2} \right)}{dV} \right]^{-1} \quad (3)$$

The donor density (N_D) is inversely proportional to the slope of a straight line of $1/C^2$ vs potential (V). Then the E_{CB} and the E_{VB} of the n-type semiconductors can be calculated from the V_{FB} using the following relation (Eqs. (4) and (5)),

$$E_{\text{CB}} = V_{\text{FB}} + kT \ln \left(\frac{N_{\text{SC}}}{N_{\text{CB}}} \right) \quad (4)$$

$$E_{\text{VB}} = E_{\text{CB}} + E_g \quad (5)$$

where N_{SC} and N_{CB} are the charge density states at the space charge layer and the conduction band, respectively. As said by the equations mentioned above, the N_D , V_{FB} , E_{CB} , and E_{VB} of the as-synthesized catalysts were estimated and given in Table 2. The acquired results exhibit the $\text{Bi}_{0.5}\text{Fe}_{0.5}\text{VO}_4/\text{SCN}$ (1.241×10^{28}) nanocomposite has a higher N_D than that of BiVO_4/SCN (7.308×10^{27}), $\text{Bi}_{0.7}\text{Fe}_{0.3}\text{VO}_4/\text{SCN}$ (6.715×10^{27}), $\text{Bi}_{0.3}\text{Fe}_{0.7}\text{VO}_4/\text{SCN}$ (7.014×10^{27}), and FeVO_4/SCN (1.186×10^{28}) nanocomposites, which suggest that the enlarged carrier concentration of the photoanode could enhance the conductivity and photocatalytic efficiency. Besides, the V_{FB} of the photoanode materials were evaluated from the intercept of the Mott-Schottky plot and are approximately equivalent to the E_{CB} of the n-type semiconductors. The $V_{\text{FB}}/V_{\text{CB}}$ offsets evidence that the photoelectrochemical water oxidation reactions are thermodynamically favorable.

The doping of Fe (III) on BiVO_4 gradually shifted the V_{FB} and E_{VB} towards a positive direction varying from $(-0.53$ to $-0.44 \text{ V})$ and $(+1.90$ – $1.58 \text{ V})$ respectively. Because of the highly positive V_{FB} (-0.46 V) and E_{VB} ($+1.48 \text{ V}$) of FeVO_4 , also the fermi-levels of $\text{Bi}_x\text{Fe}_{1-x}\text{VO}_4$ ($x = 0.7, 0.5, 0.3$) are getting equilibrated and positioned in between those of BiVO_4 and FeVO_4 . According to the expressions (4) and

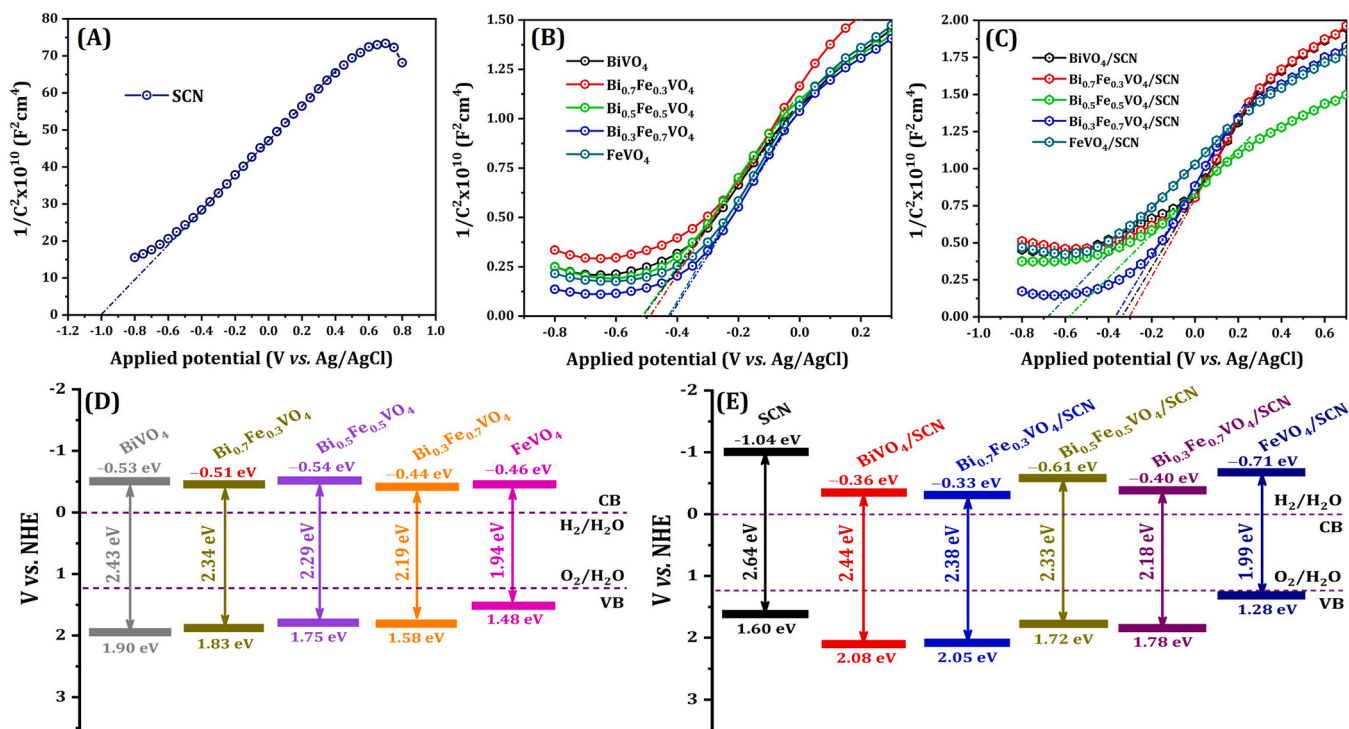


Fig. 9. The electrochemical Mott-Schottky plots of as-synthesized SCN (A), BiVO_4 , $\text{Bi}_x\text{Fe}_{1-x}\text{VO}_4$ ($x = 0.7, 0.5, 0.3$), FeVO_4 (B), BiVO_4/SCN , $\text{Bi}_x\text{Fe}_{1-x}\text{VO}_4/\text{SCN}$ ($x = 0.7, 0.5, 0.3$), FeVO_4/SCN (C), and their corresponding energy level band diagram (D and E) with respect to the V_{FB} (vs Ag/AgCl) of the Mott-Schottky plots.

Table 2

The donor densities (N_D), flat-band potentials (V_{FB}), conduction band (E_{CB}), valance band (E_{VB}), and optical bandgap energy (E_g) were calculated from the Mott-Schottky and UV-DRS analysis.

Photoanodes	N_D (cm^{-3})	V_{FB} (vs. NHE)	E_{CB} (eV)	E_{VB} (eV)	E_g (eV)
SCN	3.733×10^{26}	-1.04 V	-1.04	+1.60	2.64
BiVO_4	7.905×10^{27}	-0.53 V	-0.53	+1.90	2.43
$\text{Bi}_{0.7}\text{Fe}_{0.3}\text{VO}_4$	7.451×10^{27}	-0.51 V	-0.51	+1.83	2.34
$\text{Bi}_{0.5}\text{Fe}_{0.5}\text{VO}_4$	7.882×10^{27}	-0.54 V	-0.54	+1.75	2.29
$\text{Bi}_{0.3}\text{Fe}_{0.7}\text{VO}_4$	6.870×10^{27}	-0.44 V	-0.44	+1.58	2.19
FeVO_4	6.973×10^{27}	-0.46 V	-0.46	+1.48	1.94
BiVO_4/SCN	7.308×10^{27}	-0.36 V	-0.36	+2.08	2.44
$\text{Bi}_{0.7}\text{Fe}_{0.3}\text{VO}_4/\text{SCN}$	6.715×10^{27}	-0.33 V	-0.33	+2.05	2.38
$\text{Bi}_{0.5}\text{Fe}_{0.5}\text{VO}_4/\text{SCN}$	1.241×10^{28}	-0.61 V	-0.61	+1.72	2.33
$\text{Bi}_{0.3}\text{Fe}_{0.7}\text{VO}_4/\text{SCN}$	7.014×10^{27}	-0.40 V	-0.40	+1.78	2.18
FeVO_4/SCN	1.186×10^{28}	-0.71 V	-0.71	+1.28	1.99

(5), the E_{VB} and E_{CB} of the materials were calculated for pristine BiVO_4 , $\text{Bi}_x\text{Fe}_{1-x}\text{VO}_4$ ($x = 0.7, 0.5, 0.3$), FeVO_4 (Fig. 9D), and SCN, BiVO_4/SCN , $\text{Bi}_x\text{Fe}_{1-x}\text{VO}_4/\text{SCN}$ ($x = 0.7, 0.5, 0.3$), FeVO_4/SCN nanocomposites (Fig. 9E). Accordingly, the positive shift observed for the flat-bands of $\text{Bi}_x\text{Fe}_{1-x}\text{VO}_4/\text{SCN}$ ($x = 0.7, 0.5, 0.3$) is due to the flow of photoexcited charge carriers initiated by the built-in electric field generated at the semiconductor-electrolyte interface. Therefore, the modified band-structure offsets could drastically facilitate the donor density (e^-/h^+)

to the interface for the enriched photocatalytic and PEC water-oxidation reactions.

3.2. Photoelectrochemical oxygen evolution reactions

Photoelectrochemical OER performance of the as-synthesized different photoanode materials was evaluated by linear sweep voltammetry (LSV) measurements in the presence of 1.0 M Na_2SO_3 in 0.1 M KPi (pH=7.5) at a scanning rate of 10 mV/s (Fig. 10A). Also, the photocurrent densities (J) of the photoanodes were measured at 1.23 V (vs. RHE) in 1.0 M Na_2SO_3 in 0.1 M KPi at 10 mV/s and shown in Fig. 10B. The obtained results suggest the higher photocurrent density was exhibited by $\text{Bi}_{0.5}\text{Fe}_{0.5}\text{VO}_4/\text{SCN}$ (0.987 mA cm^{-2}) nanocomposite, and which is about 16.73, 2.94, 5.11, 3.47, 2.21, 3.23, 6.16, 2.75, 1.81, 2.14, 4.08 folds higher than that of CN (0.059 mA cm^{-2}), SCN (0.336 mA cm^{-2}), BiVO_4 (0.193 mA cm^{-2}), $\text{Bi}_{0.7}\text{Fe}_{0.3}\text{VO}_4$ (0.284 mA cm^{-2}), $\text{Bi}_{0.5}\text{Fe}_{0.5}\text{VO}_4$ (0.447 mA cm^{-2}), $\text{Bi}_{0.3}\text{Fe}_{0.7}\text{VO}_4$ (0.306 mA cm^{-2}), FeVO_4 (0.160 mA cm^{-2}), BiVO_4/SCN (0.358 mA cm^{-2}), $\text{Bi}_{0.7}\text{Fe}_{0.3}\text{VO}_4/\text{SCN}$ (0.544 mA cm^{-2}), $\text{Bi}_{0.5}\text{Fe}_{0.5}\text{VO}_4/\text{SCN}$ (0.461 mA cm^{-2}), and FeVO_4/SCN (0.242 mA cm^{-2}), respectively. Moreover, the overpotential (η_{OER}) of the different photoanodes were measured at 2 mA cm^{-2} , in 1.0 M Na_2SO_3 in 0.1 M KPi at 10 mV/s shown in Fig. 10C. In which, the $\text{Bi}_{0.5}\text{Fe}_{0.5}\text{VO}_4/\text{SCN}$ nanocomposite has smaller ($\eta_{\text{OER}} = 131 \text{ mV}$) overpotential than that of CN ($\eta_{\text{OER}} = 173 \text{ mV}$), SCN ($\eta_{\text{OER}} = 146 \text{ mV}$), BiVO_4 ($\eta_{\text{OER}} = 172 \text{ mV}$), $\text{Bi}_{0.7}\text{Fe}_{0.3}\text{VO}_4$ ($\eta_{\text{OER}} = 147 \text{ mV}$), $\text{Bi}_{0.5}\text{Fe}_{0.5}\text{VO}_4$ ($\eta_{\text{OER}} = 146 \text{ mV}$), $\text{Bi}_{0.3}\text{Fe}_{0.7}\text{VO}_4$ ($\eta_{\text{OER}} = 142 \text{ mV}$), FeVO_4 ($\eta_{\text{OER}} = 154 \text{ mV}$), BiVO_4/SCN ($\eta_{\text{OER}} = 144 \text{ mV}$), $\text{Bi}_{0.7}\text{Fe}_{0.3}\text{VO}_4/\text{SCN}$ ($\eta_{\text{OER}} = 138 \text{ mV}$), $\text{Bi}_{0.3}\text{Fe}_{0.7}\text{VO}_4/\text{SCN}$ ($\eta_{\text{OER}} = 141 \text{ mV}$), and FeVO_4/SCN ($\eta_{\text{OER}} = 161 \text{ mV}$), respectively.

Investigating the electrochemically active surface area (ECSA) of the photoanodes is necessary to analyze a number of available active sites for electrochemical and photoelectrochemical half-cycle reactions. The ECSA of the photoanodes is evaluated using a cyclic voltammetric technique (CV) by measuring the electrochemical double-layer

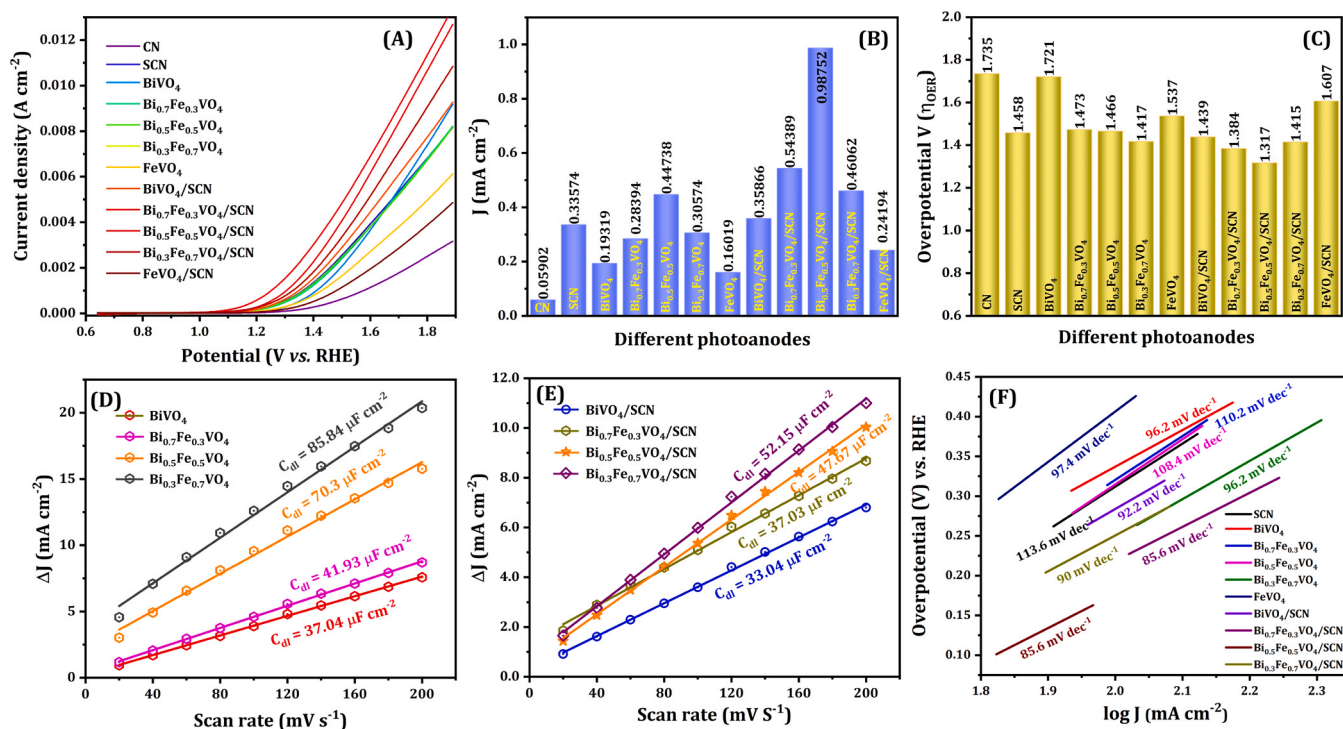


Fig. 10. Linear sweep voltammogram profiles (A), photocurrent (J) densities measured at 1.23 V (vs. RHE) (B), overpotentials measured at 2 mA cm^{-2} (η_{OER}) (C), electrochemical active surface area (ECSA) (D-E) for CN, SCN, BiVO_4 , $\text{Bi}_x\text{Fe}_{1-x}\text{VO}_4$ ($x = 0.7, 0.5, 0.3$), BiVO_4/SCN , FeVO_4 , $\text{Bi}_x\text{Fe}_{1-x}\text{VO}_4/\text{SCN}$ ($x = 0.7, 0.5, 0.3$), and FeVO_4/SCN photoanodes in the presence of 1.0 M Na_2SO_3 in 0.1 M KPi (pH = 7.5) at a scanning rate of 10 mV/s, and corresponding Tafel plots derived from LSV curves for OER (*dec = decade) (F).

capacitance (C_{dl}), in which the charge density accumulated on the electrode surface is directly proportional to the ECSA [44–46]. The CV measurements were carried out in the non-Faradaic region (0.7–0.8 V) in the presence of 1.0 M Na_2SO_3 in 0.1 M KPi at different scan rates (20–200 mV/s) (Figs. S4–S6). In accordance with the acquired C_{dl} , the ECSA of SCN ($35.64 \mu\text{F cm}^{-2}$) is 1.2 folds higher than the CN ($30.42 \mu\text{F cm}^{-2}$) (Fig. S4C). Similarly, the resultant ECSA values of $\text{Bi}_{0.7}\text{Fe}_{0.3}\text{VO}_4$ ($41.93 \mu\text{F cm}^{-2}$), $\text{Bi}_{0.5}\text{Fe}_{0.5}\text{VO}_4$ ($70.3 \mu\text{F cm}^{-2}$), and $\text{Bi}_{0.3}\text{Fe}_{0.7}\text{VO}_4$ ($85.84 \mu\text{F cm}^{-2}$) are larger than the pristine BiVO_4 ($37.04 \mu\text{F cm}^{-2}$) (Fig. 10D). Moreover, the $\text{Bi}_{0.7}\text{Fe}_{0.3}\text{VO}_4/\text{SCN}$ ($37.03 \mu\text{F cm}^{-2}$), $\text{Bi}_{0.5}\text{Fe}_{0.5}\text{VO}_4/\text{SCN}$ ($47.67 \mu\text{F cm}^{-2}$), and $\text{Bi}_{0.3}\text{Fe}_{0.7}\text{VO}_4/\text{SCN}$ ($52.15 \mu\text{F cm}^{-2}$) have larger ECSA values than the BiVO_4/SCN ($33.04 \mu\text{F cm}^{-2}$) (Fig. 10E). The more ECSA of the photoanodes can offer more electrochemical active sites for the enhanced OER reactions. The slight reduction in the ECSA of the $\text{Bi}_x\text{Fe}_{1-x}\text{VO}_4/\text{SCN}$ ($x = 0.7, 0.5, 0.3$) nanocomposites compared to the pristine $\text{Bi}_x\text{Fe}_{1-x}\text{VO}_4$ ($x = 0.7, 0.5, 0.3$) is owing to the impregnation of nanocrystals on the stacked layers of SCN. From the Tafel slopes derived from the LSV curves for OER, we can see that the $\text{Bi}_{0.5}\text{Fe}_{0.5}\text{VO}_4/\text{SCN}$ (85.6 mV dec^{-1}) has the lowest Tafel slope value than that of $\text{Bi}_{0.3}\text{Fe}_{0.7}\text{VO}_4/\text{SCN}$ (90 mV dec^{-1}), $\text{Bi}_{0.7}\text{Fe}_{0.3}\text{VO}_4/\text{SCN}$ (85.6 mV dec^{-1}), $\text{Bi}_{0.5}\text{Fe}_{0.5}\text{VO}_4$ ($108.4 \text{ mV dec}^{-1}$), $\text{Bi}_{0.7}\text{Fe}_{0.3}\text{VO}_4$ ($110.2 \text{ mV dec}^{-1}$), $\text{Bi}_{0.3}\text{Fe}_{0.7}\text{VO}_4$ (96.2 mV dec^{-1}), and SCN ($113.6 \text{ mV dec}^{-1}$) catalysts. Thus, the lower Tafel slope value of the $\text{Bi}_{0.5}\text{Fe}_{0.5}\text{VO}_4/\text{SCN}$ nanocomposite is attributed to the higher photoelectrochemical OER catalytic activity.

Moreover, the photostability of the $\text{Bi}_{0.5}\text{Fe}_{0.5}\text{VO}_4/\text{SCN}$ nanocomposite was measured by amperometric photocurrent analysis shown in Fig. S7. The main problem encountered during the photoelectrochemical OER in the presence of $\text{Bi}_x\text{Fe}_{1-x}\text{VO}_4$ material is stability. The photocurrent stability of $\text{Bi}_{0.5}\text{Fe}_{0.5}\text{VO}_4$ is relatively poor. Only 55.58% of the initial photocurrent was left after half an hour of light irradiation. The gradual decrease in the photocurrent was due to the V^{5+} dissolution into the electrolyte solution and oxidation products on the surface of the photoelectrode (O_2), which play a role as recombination centers [47]. To avoid the material dissolution, several electrocatalysts,

such as RhO_2 , Co-Pi, and Co_3O_4 , are also loaded onto the surface of BiVO_4 photoanodes, which also helps to reduce the bias-potential and improves the PEC stability [48–50]. Thus, the results show that the $\text{Bi}_{0.5}\text{Fe}_{0.5}\text{VO}_4/\text{SCN}$ nanocomposite is an excellent candidate for the photoelectrochemical OER activities due to the suitable CB and VB potentials, high electrochemical active surface area (ECSA) for surface redox reactions, and effective photogenerated charge separation through the type-II heterojunction formation between SCN and $\text{Bi}_{0.5}\text{Fe}_{0.5}\text{VO}_4$.

3.3. Photocatalytic degradation of ROX

In addition, the photocatalytic activity of the as-synthesized photocatalysts under visible-light irradiation was confirmed by the photodegradation of 4-hydroxy-3-nitrophenylarsonic acid (ROX) in an aqueous solution. About 100 mL of 50 ppm roxarsone was mixed with 50 mg of photocatalyst and stirred magnetically for 30 min in dark conditions to attain the adsorption-desorption equilibrium. The reactor temperature was maintained at $\sim 25^\circ\text{C}$ using a circulating water system. Therefore, to examine the photo-oxidation of ROX, the UV–Vis absorption spectra of ROX were monitored as a function of time (t). Fig. 11A shows the decrement in the UV–Vis spectra of ROX. The absorption bands at 220, 268, and 335 nm originated from the hydroxyl group, nitro-group, and aromatic ring present in the ROX, respectively. When the photocatalytic system was exposed to visible light, the intensities of these absorption bands decreased and thus indicating that the hydroxyl, nitro, and aromatic groups were effectively deformed in the presence of visible light and photocatalysts. Despite the arsenic group present in the ROX molecule not having a corresponding UV–Vis absorption band, at the end of the photodegradation of ROX reaction, these organoarsenic groups are mineralized into inorganic (As^{3+} , and As^{5+}) arsenic species [51–53]. As seen in Fig. 12, As(V) was the dominant inorganic arsenic species formed during the photodegradation of ROX, while As(III) was negligible. The XPS analysis shows that the presence of inorganic As(III) and As(V) accounted for 85.6% of the ROX

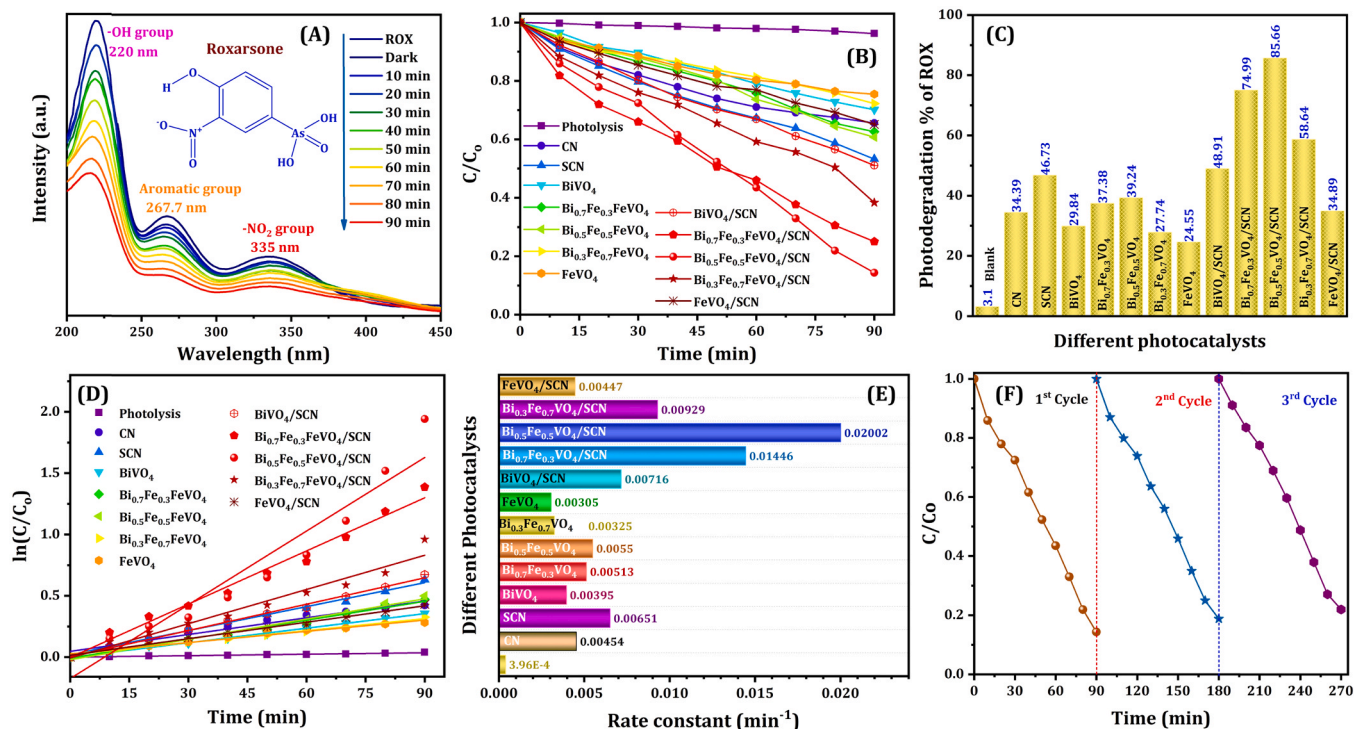


Fig. 11. UV–Vis absorption spectra for the photodegradation of ROX (A), The plot of C/C_0 vs time for different photocatalysts (B), The degradation % of ROX in the presence of different photocatalysts under visible-light irradiation (C), The pseudo-first-order kinetics plot for the photodegradation of ROX (D) and rate constants (k) in the presence of as-synthesized photocatalysts (E), and the recycling stability of $\text{Bi}_{0.5}\text{Fe}_{0.5}\text{VO}_4/\text{SCN}$ nanocomposite for three successful reaction cycles.

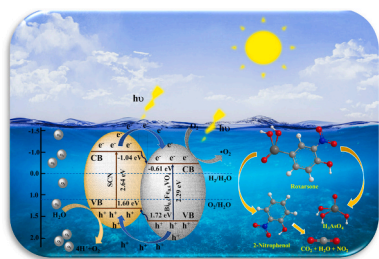


Fig. 12. Schematic illustration of the type-II heterojunction photocatalytic charge transfer mechanism on $\text{Bi}_{0.5}\text{Fe}_{0.5}\text{VO}_4/\text{SCN}$ nanocomposite towards the degradation of ROX and OER.

degradation, representing that organic arsenic substituent was mostly mineralized to inorganic arsenic species, predominantly As(V) (Fig. S8). Furthermore, As(V) can be removed from water by adsorption or coagulation. In this perspective, several synthetic iron (hydro)oxides and naturally occurring iron oxide materials such as goethite, ferrihydrite, akaganeite and hematite have been widely used as adsorbent substrates to remove inorganic arsenic species from the aqueous phase after the photodegradation experiments [54,55]. Due to the strong affinity and high selectivity towards inorganic arsenic species, these iron (hydro)oxides exhibit enhanced arsenic species immobilization efficiencies, particularly for As(V), accompanied by the advantages of low cost and extensive availability. Contrarily, due to the low affinity, the iron-based adsorbents exhibit low removal efficiency for As(III) via simple adsorption [56,57]. Hence, the adsorption treatment mentioned above by iron oxide is anticipated to completely remove the 'As' toxicity during the photodegradation of ROX.

Fig. 11B shows the relationship between C/C_0 and the degradation time of different photocatalysts. Among them, $\text{Bi}_{0.5}\text{Fe}_{0.5}\text{VO}_4/\text{SCN}$ nanocomposite exhibits a higher photodegradation efficiency (85.66%) under 90 min of light irradiation. The photodegradation efficiency of $\text{Bi}_{0.5}\text{Fe}_{0.5}\text{VO}_4/\text{SCN}$ nanocomposite is 22.54, 2.49, 1.83, 2.87, 2.29, 2.18, 3.08, 3.48, 1.75, 1.14, 1.46, and 2.45 folds higher than that of blank (3.1%), CN (34.39%), SCN (46.73%), BiVO_4 (29.84%), $\text{Bi}_{0.7}\text{Fe}_{0.3}\text{VO}_4$ (37.38%), $\text{Bi}_{0.5}\text{Fe}_{0.5}\text{VO}_4$ (39.24%), $\text{Bi}_{0.3}\text{Fe}_{0.7}\text{VO}_4$ (27.74%), FeVO_4 (24.55%), BiVO_4/SCN (48.91%), $\text{Bi}_{0.7}\text{Fe}_{0.3}\text{VO}_4/\text{SCN}$ (74.99%), $\text{Bi}_{0.3}\text{Fe}_{0.7}\text{VO}_4/\text{SCN}$ (58.64%), and FeVO_4/SCN (34.89%) samples, respectively (Fig. 11C). The obtained results suggest that $\text{Bi}_x\text{Fe}_{1-x}\text{VO}_4/\text{SCN}$ nanocomposites exhibit enhanced photocatalytic behavior than the unmodified pristine $\text{Bi}_x\text{Fe}_{1-x}\text{VO}_4$, SCN samples, owing to the following factors: (i) absorbance of a large range of light irradiation, (ii) the formation of heterojunction (type-II) enables higher photoinduced charge separation, and interfacial transfer, (iii) significantly reduced recombination rate of charge carriers, (iv) more active sites of the nanocomposite photocatalyst for the surface redox reaction, and (v) sufficient band-edge positions/potentials of the nanocomposites for high reaction rates.

As shown in Fig. 11D, the relationship between $\ln(C/C_0)$ and degradation time illustrates the pseudo-first-order kinetics (Eq. (6)) of ROX photodegradation in the presence of $\text{Bi}_x\text{Fe}_{1-x}\text{VO}_4/\text{SCN}$ nanocomposites.

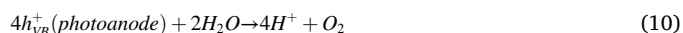
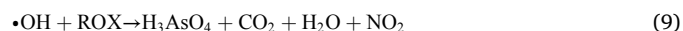
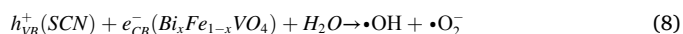
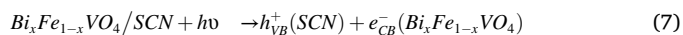
$$-\ln\left(\frac{C}{C_0}\right) = k_{\text{app}} \times t \quad (6)$$

where C_0 is the initial concentration of ROX ($t = 0$); C is the concentration of ROX at the time (t); k_{app} is the rate constant of the photodegradation reaction, and t is reaction time or irradiation time. For the photodegradation of ROX, the $\text{Bi}_{0.5}\text{Fe}_{0.5}\text{VO}_4/\text{SCN}$ nanocomposite exhibits higher rate constant (k) of $2.0 \times 10^{-2} \text{ min}^{-1}$, and which is 50.55, 4.41, 3.07, 5.07, 3.90, 3.64, 6.16, 6.56, 2.79, 1.38, 2.15, and 4.48 times more than that of blank ($3.9 \times 10^{-4} \text{ min}^{-1}$), CN ($4.5 \times 10^{-3} \text{ min}^{-1}$), SCN ($6.5 \times 10^{-3} \text{ min}^{-1}$), BiVO_4 ($3.9 \times 10^{-3} \text{ min}^{-1}$), $\text{Bi}_{0.7}\text{Fe}_{0.3}\text{VO}_4$ (5.1×10^{-3}

min^{-1}), $\text{Bi}_{0.5}\text{Fe}_{0.5}\text{VO}_4$ ($5.5 \times 10^{-3} \text{ min}^{-1}$), $\text{Bi}_{0.3}\text{Fe}_{0.7}\text{VO}_4$ ($3.2 \times 10^{-3} \text{ min}^{-1}$), FeVO_4 ($3.0 \times 10^{-3} \text{ min}^{-1}$), BiVO_4/SCN ($7.2 \times 10^{-3} \text{ min}^{-1}$), $\text{Bi}_{0.7}\text{Fe}_{0.3}\text{VO}_4/\text{SCN}$ ($1.4 \times 10^{-2} \text{ min}^{-1}$), $\text{Bi}_{0.3}\text{Fe}_{0.7}\text{VO}_4/\text{SCN}$ ($9.3 \times 10^{-3} \text{ min}^{-1}$), and FeVO_4/SCN ($4.5 \times 10^{-3} \text{ min}^{-1}$) nanocomposites (Fig. 11E). Also, the preciseness of the pseudo-first-order kinetics of the photodegradation reaction can be confirmed by the correlation coefficient (R^2) obtained from the linear fitting equation, and the R^2 values of all correspondent photocatalysts are equal to one.

3.4. Photocatalytic mechanism for PEC water-splitting and photodegradation of ROX

According to the UV-DRS and Mott-Schottky results, the bandgap energies and the valance band-conduction band potentials of as-synthesized photocatalysts were calculated, respectively (Figs. 2 and 9). The photogenerated charge transfer mechanism was proposed concerning the CB and VB edges of the SCN and $\text{Bi}_x\text{Fe}_{1-x}\text{VO}_4$ ($x = 0.7, 0.5, 0.3$). From the above analysis, the VB and CB (vs NHE) of SCN, $\text{Bi}_{0.7}\text{Fe}_{0.3}\text{VO}_4$, $\text{Bi}_{0.5}\text{Fe}_{0.5}\text{VO}_4$, $\text{Bi}_{0.3}\text{Fe}_{0.7}\text{VO}_4$ samples are calculated to be ($-1.04 \text{ eV}/+1.90 \text{ eV}$), ($-0.51 \text{ eV}/+1.83 \text{ eV}$), ($-0.54 \text{ eV}/+1.75 \text{ eV}$), and ($-0.46 \text{ eV}/+1.48 \text{ eV}$), respectively. Hence, the VB and CB potentials of $\text{Bi}_{0.7}\text{Fe}_{0.3}\text{VO}_4$ and $\text{Bi}_{0.5}\text{Fe}_{0.5}\text{VO}_4$ are more positive and less negative than the SCN. Consequently, the photoexcited electrons in the CB of SCN were transferred to the CB of $\text{Bi}_{0.7}\text{Fe}_{0.3}\text{VO}_4$, $\text{Bi}_{0.5}\text{Fe}_{0.5}\text{VO}_4$ heterostructures. Meanwhile, the photogenerated holes in the VB of $\text{Bi}_{0.7}\text{Fe}_{0.3}\text{VO}_4$, $\text{Bi}_{0.5}\text{Fe}_{0.5}\text{VO}_4$ heterostructures were transferred to the VB of SCN. Therefore, the photogenerated carriers in the $\text{Bi}_{0.7}\text{Fe}_{0.3}\text{VO}_4/\text{SCN}$ and $\text{Bi}_{0.5}\text{Fe}_{0.5}\text{VO}_4/\text{SCN}$ heterojunctions follow the staggered type-II charge transfer mechanism (Fig. 12) [58,59]. Conversely, the charge transfer process in the $\text{Bi}_{0.3}\text{Fe}_{0.7}\text{VO}_4/\text{SCN}$ heterojunction follows the straddling type-I mechanism. This is because the VB ($+1.48 \text{ eV}$) and CB (-0.46 eV) potentials of the $\text{Bi}_{0.3}\text{Fe}_{0.7}\text{VO}_4$ heterostructure are less than the VB and CB of SCN, respectively. Compared to the type-II $\text{Bi}_{0.5}\text{Fe}_{0.5}\text{VO}_4/\text{SCN}$ heterojunction, this type-I $\text{Bi}_{0.3}\text{Fe}_{0.7}\text{VO}_4/\text{SCN}$ heterojunction provides low separation and high charge recombination rates. In addition, the XPS, EIS, and transient photocurrent results also evidence the type-I & II charge transfer processes that occurred on the different $\text{Bi}_x\text{Fe}_{1-x}\text{VO}_4/\text{SCN}$ heterojunctions. The photocatalytic oxidation of ROX and PEC oxygen-evolution reaction over the $\text{Bi}_x\text{Fe}_{1-x}\text{VO}_4/\text{SCN}$ heterojunction was described by the following equations (Eqs. (7)–(10)),



3.5. Stability and recyclability of the $\text{Bi}_{0.5}\text{Fe}_{0.5}\text{VO}_4/\text{SCN}$ nanocomposite

The recycling stability of $\text{Bi}_{0.5}\text{Fe}_{0.5}\text{VO}_4/\text{SCN}$ nanocomposite towards the photocatalytic degradation of ROX was studied and shown in Fig. 11F. The used photocatalysts were recovered by centrifugation, then washed and dried for the next reaction cycle. The obtained results show the photocatalytic degradation efficiency of the $\text{Bi}_{0.5}\text{Fe}_{0.5}\text{VO}_4/\text{SCN}$ nanocomposite has lost by about 7.64% (78.02%) from its initial 85.66% efficiency after the three successful photocatalytic reaction cycles. The crystallite and morphological changes of the recycled $\text{Bi}_{0.5}\text{Fe}_{0.5}\text{VO}_4/\text{SCN}$ nanocomposite were further analyzed by XRD, TEM, and EDX after the successful reaction cycles (Fig. S9). The obtained results demonstrate the higher crystallite stability of the as-synthesized $\text{Bi}_{0.5}\text{Fe}_{0.5}\text{VO}_4/\text{SCN}$ photo(electro)catalyst. Hence, the recycling experiments prove the excellent stability of the $\text{Bi}_{0.5}\text{Fe}_{0.5}\text{VO}_4/\text{SCN}$ type-II heterojunction

nanocomposite towards sustainable environmental remediation and energy production applications.

4. Conclusion

In conclusion, hydrothermally synthesized mixed-phase (Bi and Fe) $\text{Bi}_x\text{Fe}_{1-x}\text{VO}_4$ heterostructures with different proportions ($x = 0.7; 0.5; 0.3$) have shown expanded visible-light absorption, enriched photo-generated charge carrier separation and transfer efficiencies. The as-prepared $\text{Bi}_x\text{Fe}_{1-x}\text{VO}_4$ heterostructures were impregnated on SCN using the total solvent evaporation and impregnation technique. Also, the indirect bandgap energy of $\text{Bi}_x\text{Fe}_{1-x}\text{VO}_4$ decreases with increasing Fe ratio, and $\text{Bi}_{0.5}\text{Fe}_{0.5}\text{VO}_4$ mixed phase has the optimum bandgap, excellent photogenerated charge separation and transfer efficiency than that of BiVO_4 , FeVO_4 , and $\text{Bi}_x\text{Fe}_{1-x}\text{VO}_4$ ($x = 0.7; 0.3$ wt%) nanocomposites. Thus, $\text{Bi}_{0.5}\text{Fe}_{0.5}\text{VO}_4/\text{SCN}$ nanocomposite results in 85.66% of ROX photodegradation within 90 mins under visible-light irradiation and the photocatalytic efficiency of the $\text{Bi}_{0.5}\text{Fe}_{0.5}\text{VO}_4/\text{SCN}$ nanocomposite is about 2.49, 2.87, 3.48 folds higher than that of pristine g-C₃N₄, BiVO_4 , and FeVO_4 samples, respectively. The photoelectrochemical OER results suggest the higher photocurrent density at 1.23 V (vs NHE) was achieved by $\text{Bi}_{0.5}\text{Fe}_{0.5}\text{VO}_4/\text{SCN}$ (0.987 mA cm^{-2}) nanocomposite, and which is 16.73, 5.11, and 6.16 times higher than that of CN (0.059 mA cm^{-2}), BiVO_4 (0.193 mA cm^{-2}), and FeVO_4 (0.160 mA cm^{-2}), respectively. The XPS and photoelectrochemical (PEC) analysis depict the higher donor densities and excellent charge separation possessions of the $\text{Bi}_{0.5}\text{Fe}_{0.5}\text{VO}_4/\text{SCN}$ nanocomposite by type-II heterojunction. Besides, the excellent optoelectronic properties and cyclic stability of the $\text{Bi}_{0.5}\text{Fe}_{0.5}\text{VO}_4/\text{SCN}$ nanocomposite prove it to be the robust photo (electro)catalyst for environmental remediation and energy production applications.

CRedit authorship contribution statement

Sridharan Balu: Conceptualization, Methodology, Validation, Investigation, Writing – original draft. **Yi-Lun Chen:** Methodology, Formal analysis. **Shih-Wen Chen:** Validation, Investigation, Formal analysis. **Thomas C.-K. Yang:** Conceptualization, Methodology, Validation, Resources, Supervision, Funding acquisition, Writing – review & editing.

Declaration of Competing Interest

The authors declare that they have no known competing financial interests or personal relationships that could have appeared to influence the work reported in this paper.

Acknowledgments

The authors thank Precision Analysis and Materials Research Centre (PAMRC), National Taipei University of Technology (NTUT), Taipei, Taiwan, for providing all instrument facilities for this work. This research was funded by the M-ERA.NET project “CatWatSplit” (Ref. No. project8168) and the Ministry of Science and Technology, Taiwan (MOST, Project No. 110-2923-E-027-001-MY3). The authors also thank Dr Pitchaimani Veerakumar & Dr Sangili Arumugam, National Taiwan University (NTU), Taipei, Taiwan, for helping with photocatalytic experiments.

Appendix A. Supplementary material

Supplementary data associated with this article can be found in the online version at [doi:10.1016/j.apcatb.2021.120852](https://doi.org/10.1016/j.apcatb.2021.120852).

References

- [1] Y.W. Phuan, W.-J. Ong, M.N. Chong, J.D. Ocon, Prospects of electrochemically synthesized hematite photoanodes for photoelectrochemical water splitting: a review, *J. Photochem. Photobiol. C* 33 (2017) 54–82.
- [2] D.K. Lee, D. Lee, M.A. Lumley, K.-S. Choi, Progress on ternary oxide-based photoanodes for use in photoelectrochemical cells for solar water splitting, *Chem. Soc. Rev.* 48 (2019) 2126–2157.
- [3] T.L. LeValley, A.R. Richard, M. Fan, The progress in water gas shift and steam reforming hydrogen production technologies – a review, *Int. J. Hydrog. Energy* 39 (2014) 16983–17000.
- [4] D.R. Palo, Methanol steam reforming for hydrogen production, *Chem. Rev.* 107 (2007) 3992–4021.
- [5] L.J. Minggu, W.R.W. Daud, M.B. Kassim, An overview of photocells and photoreactors for photoelectrochemical water splitting, *Int. J. Hydrog. Energy* 35 (2010) 5233–5244.
- [6] Y. Li, J.Z. Zhang, Hydrogen generation from photoelectrochemical water splitting based on nanomaterials, *Laser Photonics Rev.* 4 (2010) 517–528.
- [7] J. Joy, J. Mathew, S.C. George, Nanomaterials for photoelectrochemical water splitting – review, *Int. J. Hydrog. Energy* 43 (2018) 4804–4817.
- [8] B. Chen, Q. Liu, A. Popowich, S. Shen, X. Yan, Q. Zhang, X.-F. Li, M. Weinfeld, W. R. Cullen, C. Le, Therapeutic and analytical applications of arsenic binding to proteins, *Metallomics* 7 (2015) 39–55.
- [9] H.J. Iland, J.F. Seymour, Role of arsenic trioxide in acute promyelocytic leukemia, *Curr. Treat. Options Oncol.* 14 (2013) 170–184.
- [10] J. Matschullat, Arsenic in the geosphere—a review, *Sci. Total Environ.* 249 (2000) 297–312.
- [11] Y. Qi, R.J. Donahoe, The environmental fate of arsenic in surface soil contaminated by historical herbicide application, *Sci. Total Environ.* 405 (2008) 246–254.
- [12] S. Mandal, M.K. Sahu, R.K. Patel, Adsorption studies of arsenic(III) removal from water by zirconium polyacrylamide hybrid material (ZrPACM-43), *Water Resour. Ind.* 4 (2013) 51–67.
- [13] S. Amrose, A. Gadgil, V. Srinivasan, K. Kowolik, M. Muller, J. Huang, R. Kostecki, Arsenic removal from groundwater using iron electrocoagulation: effect of charge dosage rate, *J. Environ. Sci. Health* 48 (2013) 1019–1030.
- [14] D. Lu, F. Ji, W. Wang, S. Yuan, Z.-H. Hu, T. Chen, Adsorption and photocatalytic decomposition of roxarsone by TiO₂ and its mechanism, *Environ. Sci. Pollut. Res.* 21 (2014) 8025–8035.
- [15] D. Kim, J. Lee, J. Ryu, K. Kim, W. Choi, Arsenite oxidation initiated by the UV photolysis of nitrite and nitrate, *Environ. Sci. Technol.* 48 (2014) 4030–4037.
- [16] K. Acuna, J. Yanez, S. Ranganathan, E. Ramirez, J.P. Cuevas, H.D. Mansilla, P. Santander, Photocatalytic degradation of roxarsone by using synthesized ZnO nanoplates, *Sol. Energy* 157 (2017) 335–341.
- [17] M. Zhang, Y. Ma, D. Friedrich, R.V.D. Krol, L.H. Wong, F.F. Abdi, Elucidation of the opto-electronic and photoelectrochemical properties of FeVO₄ photoanodes for solar water oxidation, *J. Mater. Chem. A* 6 (2018) 548–555.
- [18] H. Liu, R. Nakamura, Y. Nakato, A visible-light responsive photocatalyst, BiZn[sub 2]VO[sub 6], for efficient oxygen photoevolution from aqueous particulate suspensions, *Electrochem. Solid-State Lett.* 9 (5) (2006) G187–G190.
- [19] Y. Murakami, M. Ikarashi, M. Hashizume, A.Y. Nosaka, Y. Nosaka, Laser ablation of the photocatalytic BiVO[sub 4] and BiZn[sub 2]VO[sub 6] powders in water and their photocurrent properties, *Electrochem. Solid-State Lett.* 11 (2) (2008) H42–H46.
- [20] Z. Ding, Y. Fu, Z. Xie, Z. Li, A polymeric complex method to nanocrystalline BiCu₂VO₆ with visible light photocatalytic activity, *Mater. Lett.* 65 (2011) 460–463.
- [21] H. Liu, R. Nakamura, Y. Nakato, Bismuth-copper vanadate BiCu₂VO₆ as a novel photocatalyst for efficient visible-light-driven oxygen evolution, *ChemPhysChem* 6 (2005) 2499–2502.
- [22] M. Zhang, H.K. Pham, Y. Fang, Y.F. Tay, F.F. Abdi, L.H. Wong, The synergistic effect of cation mixing in mesoporous BiFe_{1-x}VO₄ heterojunction photoanodes for solar water splitting, *J. Mater. Chem. A* 7 (2019) 14816–14824.
- [23] S.C. Yan, Z.S. Li, Z.G. Zou, Photodegradation performance of g-C₃N₄ fabricated by directly heating melamine, *Langmuir* 25 (17) (2009) 10397–10401.
- [24] L. Pavasaryte, S. Balu, T.C.-K. Yang, Synthesis of sol–gel derived holmium aluminium garnet on exfoliated g-C₃N₄: a novel visible-light-driven Z-scheme photocatalyst for the degradation of sunset yellow FCF, *J. Mater. Sci. Mater. Electron.* 30 (2019) 20132–20143.
- [25] K. Wang, Q. Li, B. Liu, B. Cheng, W. Ho, J. Yu, *Appl. Catal. B Environ.* 176–177 (2015) 44–52.
- [26] J. Huang, D. Li, R. Li, Q. Zhang, T. Chen, H. Liu, Y. Liu, W. Lv, G. Liu, An efficient metal-free phosphorus and oxygen co-doped g-C₃N₄ photocatalyst with enhanced visible light photocatalytic activity for the degradation of fluoroquinolone antibiotics, *Chem. Eng. J.* 374 (2019) 242–253.
- [27] T.M. Shamsabadi, B.-K. Lee, Photocatalytic H₂ evolution and CO₂ reduction over phosphorus-doped g-C₃N₄ nanostructures: electronic, optical, and surface properties, *Renew. Sustain. Energy Rev.* 130 (2020), 109957.
- [28] S. Cao, B. Fan, Y. Feng, H. Chen, F. Jiang, X. Wang, Sulfur-doped g-C₃N₄ nanosheets with carbon vacancies: general synthesis and improved activity for simulated solar-light photocatalytic nitrogen fixation, *Chem. Eng. J.* 353 (2018) 147–156.
- [29] S. Balu, Y.-L. Chen, T.C.-K. Yang, J.-N. Chen, S.-W. Chen, Effect of ultrasound-induced hydroxylation and exfoliation on P90-TiO₂/g-C₃N₄ hybrids with enhanced optoelectronic properties for visible-light photocatalysis and electrochemical sensing, *Ceram. Int.* 46 (2020) 18002–18018.

- [30] G. Liu, X. Qiao, M.A. Gondal, Y. Liu, K. Shen, Q. Xu, Comparative study of pure g-C₃N₄ and sulfur-doped g-C₃N₄ catalyst performance in photo-degradation of persistent pollutant under visible light, *J. Nanosci. Nanotechnol.* 18 (2018) 4142–4154.
- [31] W. Wang, J. Wang, Z. Wang, X. Wei, L. Liu, Q. Ren, W. Gao, Y. Liang, H. Shi, p-n junction CuO/BiVO₄ heterogeneous nanostructures: synthesis and highly efficient visible-light photocatalytic performance, *Dalton Trans.* 43 (2014) 6735–6743.
- [32] W. Wang, X. Huang, S. Wu, Y. Zhou, L. Wang, H. Shi, Y. Liang, B. Zou, Preparation of p-n junction Cu₂O/BiVO₄ heterogeneous nanostructures with enhanced visible-light photocatalytic activity, *Appl. Catal. B Environ.* 134–135 (2013) 293–301.
- [33] Q. Wang, Z. Liu, Q. Lu, E. Guo, M. Wei, Fabrication of direct Z-scheme α-Fe₂O₃/FeVO₄ nanobelts with Enhanced Photoelectrochemical Performance, *ChemistrySelect* 3 (2018) 809–815.
- [34] G. Bera, V.R. Reddy, P. Rambabu, P. Mal, P. Das, N. Mohapatra, G. Padmaja, G. R. Turpu, Triclinic–monoclinic–orthorhombic (T–M–O) structural transitions in phase diagram of FeVO₄–CrVO₄ solid solutions, *J. Appl. Phys.* 122 (2017), 115101.
- [35] K. Wang, Q. Li, B. Liu, B. Cheng, W. Ho, J. Yu, *Appl. Catal. B Environ.* 176–177 (2015) 44–52.
- [36] S. Fang, S. Xue, C. Wang, G. Wang, X. Wang, Q. Liang, Z. Li, S. Xu, Fabrication and characterization of CdS/BiVO₄ nanocomposites with efficient visible light driven photocatalytic activities, *Ceram. Int.* 42 (2016) 4421–4428.
- [37] R. Yang, Z. Zhu, C. Hu, S. Zhong, L. Zhang, B. Liu, W. Wang, One-step preparation (3D/2D/2D) BiVO₄/FeVO₄@rGO heterojunction composite photocatalyst for the removal of tetracycline and hexavalent chromium ions in water, *Chem. Eng. J.* 390 (2020), 124522.
- [38] S. Balu, Y.-L. Chen, R.-C. Juang, T.C.-K. Yang, J.C. Juan, Morphology-controlled synthesis of α-Fe₂O₃ nanocrystals impregnated on g-C₃N₄-SO₃H with ultrafast charge separation for photoreduction of Cr (VI) under visible light, *Environ. Pollut.* 267 (2020), 115491.
- [39] L. Ge, Novel Pd/BiVO₄ composite photocatalysts for efficient degradation of methyl orange under visible light irradiation, *Mater. Chem. Phys.* 107 (2008) 465–470.
- [40] S.K. Biswas, J.O. Baeg, Enhanced photoactivity of visible light responsive W incorporated FeVO₄ photoanode for solar water splitting, *Int. J. Hydrog. Energy* 38 (2013) 14451–14457.
- [41] F.L. Formal, K. Sivula, M. Grätzel, The transient photocurrent and photovoltage behavior of a hematite photoanode under working conditions and the influence of surface treatments, *J. Phys. Chem. C* 116 (2012) 26707–26720.
- [42] Y.-H. Chiu, K.-D. Chang, Y.-J. Hsu, Plasmon-mediated charge dynamics and photoactivity enhancement for Au-decorated ZnO nanocrystals, *J. Mater. Chem. A* 6 (2018) 4286–4296.
- [43] P. Veerakumar, A. Sangili, K. Saranya, A. Pandikumar, K.-C. Lin, Palladium and silver nanoparticles embedded on zinc oxide nanostars for photocatalytic degradation of pesticides and herbicides, *Chem. Eng. J.* 410 (2021), 128434.
- [44] W. Lv, J. Bei, R. Zhang, W. Wang, F. Kong, L. Wang, W. Wang, Bi₂O₂CO₃ nanosheets as electrocatalysts for selective reduction of CO₂ to formate at low overpotential, *ACS Omega* 2 (2017) 2561–2567.
- [45] H.L.S. Santos, P.G. Corradini, M. Medina, J.A. Dias, L.H. Mascaro, NiMo–NiCu inexpensive composite with high activity for hydrogen evolution reaction, *ACS Appl. Mater. Interfaces* 12 (2020) 17492–17501.
- [46] P. Connor, J. Schuch, B. Kaiser, W. Jaegermann, The determination of electrochemical active surface area and specific capacity revisited for the system MnOx as an oxygen evolution catalyst, *Z. Phys. Chem.* 234 (5) (2020) 979–994.
- [47] Z. Li, W. Luo, M. Zhang, J. Feng, Z. Zou, Photoelectrochemical cells for solar hydrogen production: current state of promising photoelectrodes, methods to improve their properties, and outlook, *Energy Environ. Sci.* 6 (2013) 347–370.
- [48] W.J. Luo, Z.S. Yang, Z.S. Li, J.Y. Zhang, J.G. Liu, Z.Y. Zhao, Z.Q. Wang, S.C. Yan, T. Yu, Z.G. Zou, Solar hydrogen generation from seawater with a modified BiVO₄ photoanode, *Energy Environ. Sci.* 4 (2011) 4046–4051.
- [49] F.F. Abdi, R. van de Krol, Nature and light dependence of bulk recombination in Co-Pi-catalyzed BiVO₄ photoanodes, *J. Phys. Chem. C* 116 (2012) 9398–9404.
- [50] M. Long, W. Cai, H. Kisch, Visible light induced photoelectrochemical properties of n-BiVO₄ and n-BiVO₄/p-Co₃O₄, *J. Phys. Chem. C* 112 (2008) 548–554.
- [51] P. Hu, Y. Liu, B. Jiang, X. Zheng, J. Zheng, M. Wu, High-efficiency simultaneous oxidation of organoarsenic and immobilization of arsenic in fenton enhanced plasma system, *Ind. Eng. Chem. Res.* 54 (2015) 8277–8286.
- [52] W. Fu, D.-L. Lu, H. Yao, S. Yuan, W. Wang, M. Gong, Z.-H. Hu, Simultaneous roxarsone photocatalytic degradation and arsenic adsorption removal by TiO₂/FeOOH hybrid, *Environ. Sci. Pollut. Res.* 27 (2020) 18434–18442.
- [53] S. Zheng, W. Jiang, Y. Cai, D.D. Dionysiou, K.E. O'Shea, Adsorption and photocatalytic degradation of aromatic organoarsenic compounds in TiO₂ suspension, *Catal. Today* 224 (2014) 83–88.
- [54] Z. Zhao, Y. Jia, L. Xu, S. Zhao, Adsorption and heterogeneous oxidation of As(III) on ferrihydrite, *Water Res.* 45 (2011) 6496–6504.
- [55] X. Yang, L. Xia, J. Li, M. Dai, G. Yang, S. Song, Adsorption of As(III) on porous hematite synthesized from goethite concentrate, *Chemosphere* 169 (2017) 188–193.
- [56] P.L. Smedley, D.G. Kinniburgh, A review of the source, behaviour and distribution of arsenic in natural waters, *Appl. Geochem.* 17 (2002) 517–568.
- [57] S. Lata, S.R. Samadder, Removal of arsenic from water using nano adsorbents and challenges: a review, *J. Environ. Manag.* 166 (2016) 387–406.
- [58] J.S. Chang, Y.W. Phuan, M.N. Chong, J.D. Ocon, Exploration of a novel Type II 1D-ZnO nanorods/BiVO₄ heterojunction photocatalyst for water depollution, *J. Ind. Eng. Chem.* 83 (2020) 303–314.
- [59] L. Pei, H. Wang, X. Wang, Z. Xu, S. Yan, Z. Zou, Nanostructured TaON/Ta₃N₅ as a highly efficient type-II heterojunction photoanode for photoelectrochemical water splitting, *Dalton Trans.* 47 (2018) 8949–8955.